Department of Construction Sciences
Solid Mechanics

ISRN LUTFD2/TFHF-20/5235-SE(1-63)

Investigation of friction drive for night closing door

Master's Dissertation by

Sissela Svärd

Supervisors: Håkan Hallberg, Division of Solid Mechanics
Roger Dreyer, ASSA ABLOY
Sven Åsbo, ASSA ABLOY

Examiner: Mathias Wallin, Division of Solid Mechanics

Printed by Media-Tryck AB, Lund, Sweden
For information, address:
Division of Solid Mechanics, Lund University, Box 118, SE-221 00 Lund, Sweden
Webpage: www.solid.lth.se

Abstract

ASSA Abloy Entrance Systems design and manufacture automatic sliding-, swing- and revolving doors. A regular revolving door is often equipped with night closing doors on the outside, which are used to close the entrance when, for example, the store or workplace is closed for the evening. This prevents unwanted guests or litter to enter the space between the revolving door blades. This Master's thesis focus on the small driving unit that is used for driving the night closing door blades back and forth during opening and closing. The force transmission between the driving unit and the door blades is based on the friction in the contact surfaces between the different components. The dimensions of each component are very limited since the space intended for the friction drive unit is very small.

In this Master's thesis, the night closing door friction drive is studied and developed to endure the high forces that act on the components. The dimensions are evaluated by considering, for example, the Hertzian contact pressure and creep ratio. Different material- and surface treatment combinations are considered to decrease stresses and fatigue wear. Other factors, such as different profile geometries of the rollers, were considered as well, to reduce the stresses. A bearing shaft with a logarithmic profile yielded a rather good result, where the edge stresses were reduced significantly. Both steel SS 2541 with Corr-i-Dur treatment and steel SS 2940-03 with gas nitriding surface treatment had some positive effects on the fatigue life.

Literature studies and numerical finite element simulations were used to draw conclusions about the night closing door friction drive. Practical tests were also performed, but due to the Covid-19 pandemic the planned extent of these tests unfortunatly came out very limited.

Keywords: Hertzian Contact Pressure, Rolling Friction, Finite Element Analysis, Fatigue, Material.

Acknowledgements

I would like to begin to thank my two supervisors at ASSA ABLOY, Sven Åsbo and Roger Dreyer. You have been very welcoming and dedicated to helping me throughout my Master's thesis, even though the Covid-19 pandemic forced us to keep our distance. My impression of the company is very good and I hope that I can return to ASSA ABLOY sometime in the future.

I would also like to thank my supervisor at LTH, Håkan Hallberg. I am very grateful for all the support during the whole process and all the valuable feedback you have given me on the report. I am also very happy that you made me interested in solid mechanics from my very first course on the subject.

I am also very grateful for the help I received from Axel Nordin. You have answered all my questions about Ansys Workbench in the most pedagogical way. And lastly, I want to thank Jennie Walfridsson for the work you did at ASSA ABLOY before I started my Master's thesis and the very valuable input about the NCD friction drive that you provided.

Notations

R	Radius	[m]
E	Young's modulus	[MPa]
ν	Poisson's ratio	[-]
s	Creep ratio	[-]
a	Half width of contact area	[m]
c	Half width of sticking region	[m]
d	Auxiliary dimension inside of sticking region	[MPa]
R^*	Load ratio	[-]
P	Compressional force or normal force	[N]
L	Length of shafts	[m]
E_{eff}	Effective Young's modulus	[MPa]
S	Auxiliary parameter	[MPa^{-1}]
Ψ	Angle between main curvatures	[°]
θ^*	Auxiliary parameter	[°]
θ	Angle used in defining the coefficient of friction	[°]
p_{max}	Maximum Hertzian pressure	[MPa]
σ_{xx}, σ_{yy}, σ_{zz}	Normal stress in x-, y-, and z-direction	[MPa]
μ_s	Coefficient of static friction	[-]
μ_k	Coefficient of kinetic friction	[-]
μ_r	Coefficient of rolling friction	[-]
F_x	Friction force	[N]
F_R	Reaction force	[N]
ϕ	Angle between compression- and reaction force	[°]
ϵ_{xx}	Normal strain in x-direction	[-]
τ	Shear stress	[MPa]
τ_0	Maximum shear stress	[MPa]
u_x	Displacement in x-direction	[m]
$\Delta\sigma$	Stress range	[MPa]
σ_a	Stress amplitude	[MPa]
σ_m	Mean stress	[MPa]
σ_e	Endurance limit	[MPa]
σ_Y	Yield stress	[MPa]
σ_{TS}	Ultimate tensile stress	[MPa]
σ'_f	Fatigue strength coefficient	[MPa]
b	Fatigue strength exponent	[-]
ϵ_c	Ratcheting material constant	[-]
$\Delta\tilde{\epsilon}$	Average ratcheting axial strain range	[-]
$\Delta\tilde{\gamma}$	Average ratcheting shear strain range	[-]
R_a	Arithmetical mean deviation of the profile height	[μm]
N_f	Number of cycles to failure	[-]
HV	Vicker's hardness	[MPa]
σ_{Y0}	Yield strength before surface treatment	[MPa]
HV_0	Vicker's hardness before surface treatment	[MPa]

Abbreviations

NCD	Night closing door
LCF	Low cycle fatigue
HCF	High cycle fatigue

Contents

1 Introduction

1.1 Background

ASSA ABLOY Entrance Systems develop, produces and sell revolving-, sliding- and swing doors. They are all equipped with different types of automatic solutions for opening and closing.

ASSA ABLOY's revolving doors are equipped with an outer shell, in the form of a curved door. This outer door can be closed when for example the store, office or mall closes for the evening. It is called night closing door, NCD, and is there to prevent for example littering or unwanted night guests in the space between the door wings. A schematic overview of the night closing door is presented in figure 1.2 and the more exact location of the components is shown in figure 1.1.

The NCD itself is not a new feature on revolving doors. However, right now a new design of revolving doors is under development and it is found that the driving system that is currently used to guide and drive the automatic NCD is too big for the new design. Therefore, a new type of friction drive has to be developed. Since the new NCD friction drive has to be considerably smaller, but still has to sustain high stresses and repetitive loads, the requirements on material, dimensions, surface treatments and so on are much higher.

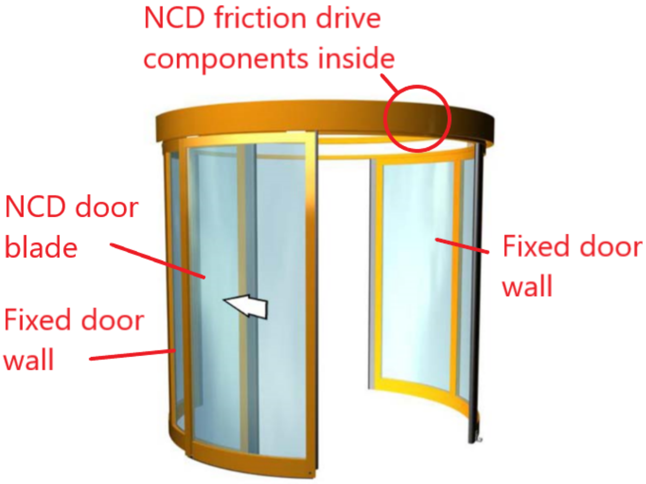

Figure 1.1: Revolving door with night closing doors in opening mode.

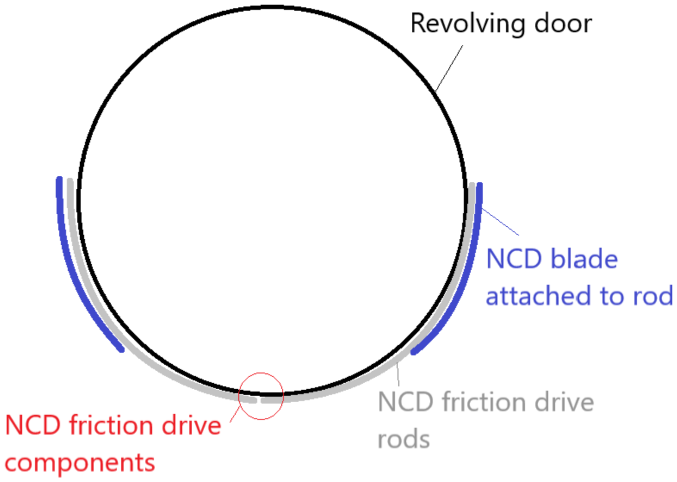

Figure 1.2: Night closing door from above and the location of the NCD friction drive.

The main structure of the NCD friction drive is already determined by ASSA ABLOY. It will consist of one cylindrical driving shaft in contact with two rods with plane surfaces. The other side of the rods will be in contact with a bearing or a bearing shaft. These two shafts will be clamped together by a compression device, see figure 1.3. The location of these components is shown in figure 1.2.

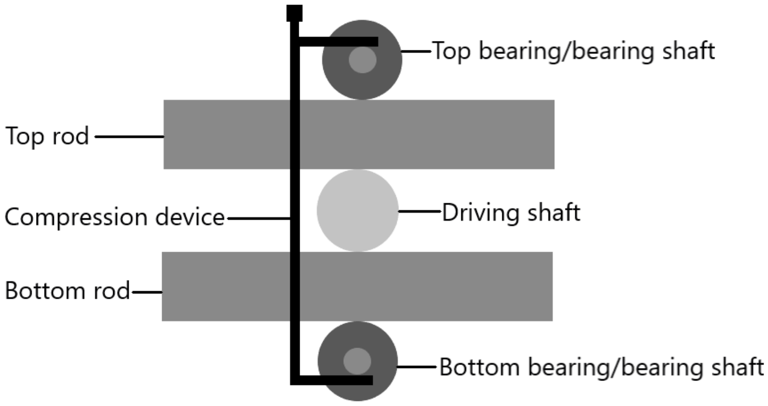

Figure 1.3: All components of the NCD friction drive seen from front of the door.

The night closing door blades are attached to the two rods and a motor is connected to the driving shaft. When the motor is running, the driving shaft is rotated and hence the rods are driven back and forth together with the door blades.

1.2 Objective

The main objective of this Master's thesis is to develop the basic construction of the friction drive to suit the new design of the revolving doors. The main focus will be on:

- Finding the right material and surface treatment that provides the desired surface roughness and hardness.
- Finding the right compression force for which the friction drive can be clamped together. The force has to provide high enough friction to avoid sliding, but low enough stresses to avoid high wear rates and fatigue. It is also requested that the friction drive will generate a horizontal force of 150 N. The reason for the 150 N limit will be explained later in section 1.4.
- Finding the right dimension of each component in the friction drive, to reduce stresses, wear and fatigue, but still providing minimal sliding. This also includes finding the correct profile for some of the components, for example circular crowning on the bearing or bearing shafts.

1.3 Methodology

The objective is to find a solution that works, not necessarily to find the ultimate solution. The methodology will consist of theoretical calculations, simulations with Ansys Workbench as well as practical tests.

The calculations and analysis will be performed using a number of theoretical expressions, such as those for Hertz's contact pressure and Coulomb's friction. Some of these expressions are not directly applicable on the NCD friction drive, but has to be modified. This is done, both based on findings in the literature and based on results from numerical simulations in Ansys Workbench.

The simulations will be made with the objective to both predict the compression force required and to analyse the stresses when the geometry of the bearing shafts are changed. Practical tests will be made to verify the simulations and to analyse the fatigue behaviour of the components.

1.4 Limitations

The NCD friction drive is, as earlier mentioned, curved to fit the revolving door. However, in the calculations and simulations, the rods that the doors are connected to will be approximated as straight. Since the majority of the calculations and observations will be focused on contact surfaces between each component and because the radii of the rods are much bigger than the radii of the three cylindrical shafts, it is not necessary to consider the curvature of the rods in the NCD friction drive.

The rods have a very small cross section compared to the length. This can lead to that the rods bend due to their own weight. This problem will not be considered to any large extent in this Master's thesis. It will be solved by ASSA ABLOY designers later, for example by adding support bearings or other components along the rods.

As previously mentioned, the NCD friction drive dimensions are limited in terms of how high and how wide/deep it can be. The absolute maximum allowed height is 52 mm. This does not, however, include only the rods and rollers, but might also include the device that is used to compress the components. Right now it is unknown how this device will be designed. Hopefully it will be designed to not take up much space over and beneath the rollers, but this kind of construction is outside the scope for this Master's thesis. The length of the rollers and width of the rods can be maximum 30 mm.

The NCD friction drive will be designed to be able to produce a horizontal force of 150 N in both directions. The reason for this is that if the NCD is closing and someone or something happens to be in the way at that moment, the doors have to quickly change direction of motion and open again to prevent any damages to the person or object. The acceleration and mass of the night closing doors corresponds to 150 N in each direction.

2 Theory

2.1 Hertzian Contact

To describe and calculate rolling contact and rolling resistance of the NCD friction drive, the concept *Hertzian contact* is introduced first.

When two bodies with arbitrary shapes are in contact with each other due to a force perpendicular to the contact surface, a normal contact problem arise [1]. A general description of this is illustrated in figure, 2.1, where normal contact occurs when $\Psi = 0$. This type of contact mechanics, where the contact between two elastic bodies with curved surfaces is described, is often called Hertzian contact mechanics after *Heinrich Hertz*, who solved the problem in 1882.

Hertz contact theory is, in the most general case, based on the assumption that the contact surface is shaped as an ellipse [2]. It is also assumed that the area of the contact surface is small in relation to both the size of the bodies and the radius of the curvature of the body in the point of contact. It is also assumed that all frictional forces are negligible.

The two bodies in contact are assumed to have the material parameters E_1, E_2, ν_1 and ν_2, which corresponds to Young's modulus and Poisson's ratio for the two respective bodies, see figure 2.1. To be able to describe the influence of the material in the contact surface region, new material parameters are introduced in terms of an effective elasticity modulus, E_{eff} [3], and the parameter S [2], which is an auxiliary parameter combining effective Poisson's ratio and Young's modulus.

$$E_{eff} = \Big(\frac{1-\nu_1}{E_1}\Big) + \Big(\frac{1-\nu_2}{E_2}\Big) \tag{2.1}$$

$$S = \frac{1}{2}\Big(\frac{1-\nu_1^2}{E_1} + \frac{1-\nu_2^2}{E_2}\Big) \tag{2.2}$$

Two other variables, A and B, are also introduced. According to [2], they are defined by

$$A+B=\frac{1}{2}\Big(\frac{1}{R_1}+\frac{1}{R_1'}+\frac{1}{R_2}+\frac{1}{R_2'}\Big) \tag{2.3}$$

and

$$B-A=\frac{1}{2}\Bigg(\Big(\frac{1}{R_1}-\frac{1}{R_1'}\Big)^2+\Big(\frac{1}{R_2}-\frac{1}{R_2'}\Big)^2+2\Big(\frac{1}{R_1}-\frac{1}{R_1'}\Big)\Big(\frac{1}{R_2}-\frac{1}{R_2'}\Big)\cos 2\Psi\Bigg)^{\frac{1}{2}} \tag{2.4}$$

Where R_1 and R_1' are the half axes of the ellipsoid body 1 and R_2 and R_2' are the half axes of body 2. Ψ is the angle between the main curvatures of the bodies, see figure 2.1. Since the contact between the bodies is assumed to be normal and purely vertical, the angle Ψ will always be zero in the application of the NCD friction drive.

A new parameter θ^* is defined from eq. (2.3) and (2.4). θ^* is used later for defining the half axes of the elliptical contact surface in the general case, see figure 2.1b.

$$\cos\theta^*=\frac{B-A}{A+B} \tag{2.5}$$

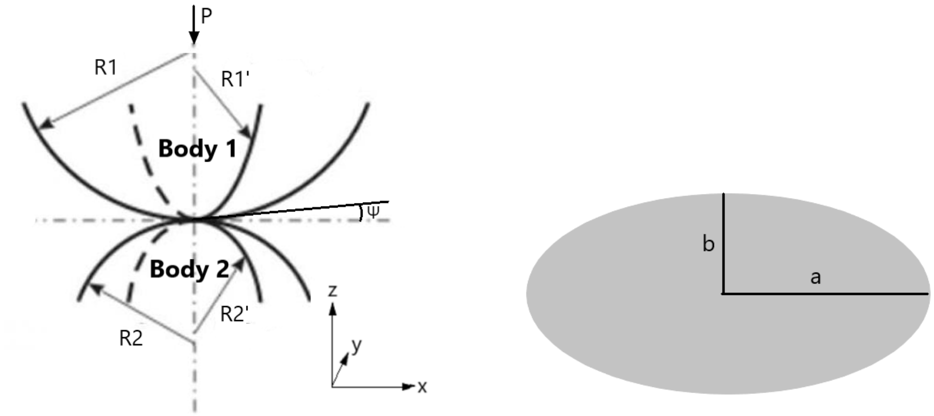

(a) General Hertzian contact (b) Contact area

Figure 2.1: Illustration of the notations and parameters used in the definition of a general Hertzian contact, together with the notations of the contact area.

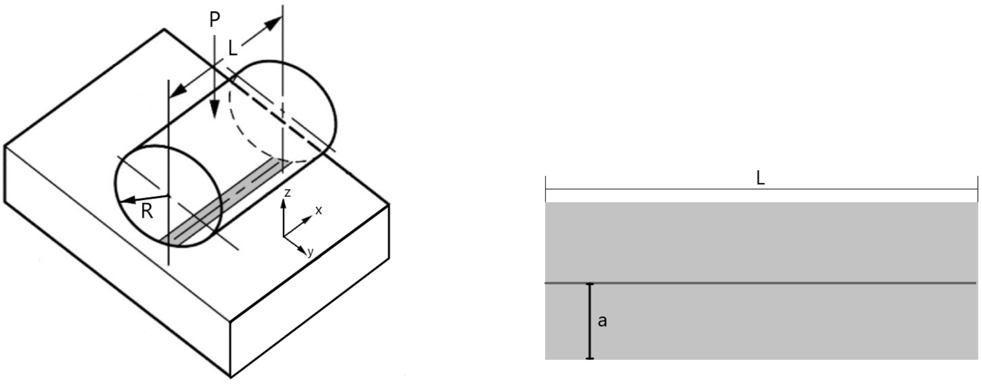

(a) Cylindrical Hertzian contact.

(b) Contact area, corresponding to the shaded region in figure a.

Figure 2.2: Illustration of the notations and parameters used in the definition of a cylindrical Hertzian contact, together with the notations of the contact area.

With the definitions from eq. (2.2) and (2.3) and following [2], the half axes of the contact surface, a and b, can be defined as

$$a = m\Big(\frac{3PS}{2(A+B)}\Big)^{\frac{1}{3}} \tag{2.6}$$

$$b = n\Big(\frac{3PS}{2(A+B)}\Big)^{\frac{1}{3}} \tag{2.7}$$

where the coefficients m and n depend on the angle θ^* from eq. (2.5). The parameters m and n are then taken from table 8.1 in Appendix A. P is the force that is acting on the upper body, bringing the two bodies to contact, see figure 2.1. One problem with this method is that the table of values for m and n are quite well defined for most of the values for θ^*, but for low values of θ^*, the variations are very high and the table degenerates [2]. It is therefore difficult to calculate the Hertzian contact pressure for slightly curved surfaces.

The pressure in the contact area is distributed as a parabolic function, where the maximum pressure, according to [2], is

$$p_{max} = \frac{3P}{2\pi ab} \tag{2.8}$$

Since the NCD friction drive in the most basic design, is composed of cylinders and plane rods, the general case of contact can be reduced to a cylinder in contact with a plane half space, see figure 2.2b. The contact surface in this case is rectangular and has a half width of a. Following [2], a is defined as

$$a = \sqrt{\frac{8PSR}{\pi L}} \tag{2.9}$$

where P is the force load, R is the radius of the cylinder and L is the contact length. The pressure, defined in eq. (2.10), is still parabolic and has the maximum pressure acting on a line along the contact surface. Inserting eq. (2.9), the pressure can also be defined as eq. (2.11). The equations for a cylinder in contact with a half plane will be most relevant for the calculations performed in this Master's thesis project. However, the general form of Hertzian contact will come in handy when alternative roller profiles are explored.

$$p_{max} = \sqrt{\frac{P}{2\pi RLS}} \tag{2.10}$$

$$p_{max} = \frac{2P}{\pi a L} \tag{2.11}$$

The stress distributions are calculated with eq. (2.12)-(2.14) for cylindrical contact, taken from [4]. It can be seen that the maximum Hertzian pressure is equal to the normal stress in both y- and z-direction at the line of contact (when z=0), see the coordinate system in figure 2.2.

$$\sigma_{xx} = -2\nu p_{max}\left(\sqrt{1+\frac{z^2}{a^2}}+\frac{z}{a}\right) \tag{2.12}$$

$$\sigma_{yy} = -p_{max}\left(\left(1+2\frac{z^2}{a^2}\right)\left(\frac{z^2}{a^2}+1\right)^{-\frac{1}{2}} - 2\frac{z}{a}\right) \tag{2.13}$$

$$\sigma_{zz} = -p_{max}\left(\frac{z^2}{a^2}+1\right)^{-\frac{1}{2}} \tag{2.14}$$

In eq. (2.12)-(2.14) it can also be seen that the stresses are limited to the near surface. In a cylindrical contact, where the half width of the contact area is for example 0.07 mm, which is the approximate case when the NCD friction drive is exposed to a 1300 N force load, the stress is only approximately 14% of p_{max} at a distance of 0.5 mm beneath the surface. Hence, it is proven that the contact stresses only occur near the surface.

2.2 Rolling Contact and Resistance

The NCD friction drive function is based on several rolling contacts between the different components, driving the rods back and forth. Regular sliding friction between two bodies can be expressed with Coulomb's friction as

$$F_x = \mu_s P \tag{2.15}$$

for a static system [1]. F_x is the friction force, μ_s is the static friction coefficient and P is the normal force. As long as $F_x < \mu_s P$ the system is static. In a similar way, the sliding friction for a dynamic system is

$$F_x = \mu_k P \tag{2.16}$$

where μ_k is the dynamic friction coefficient. It is usually smaller than μ_s, but can in many cases be approximated as $\mu_k \approx \mu_s$. The friction coefficient is a purely empirical parameter, which means that it has to be determined through experiments [5]. A very easy way to measure the static friction coefficient is to place an object on a flat surface, tilt the surface and record the angle at which the object starts to slide. This is illustrated in figure 2.3. Assuming equilibrium at that moment, see figure 2.3, the equilibrium equations yield

$$\begin{cases} mg\sin\theta - \mu_s P = 0 & (2.17) \\ P - mg\cos\theta = 0 & (2.18) \end{cases}$$

Rearranging the variables lead to the expression

$$\mu_s = \tan\theta \qquad (2.19)$$

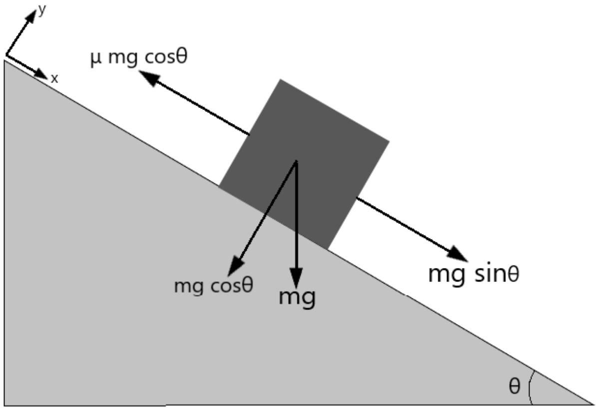

Figure 2.3: Experimental setup and forces acting on an object in equilibrium used for calculating the coefficient of friction.

This very basic experimental method will be used later during this Master's thesis to predict the compression force necessary to obtain high enough horizontal force.

The rolling friction is the resistance for a body to roll and is often expressed as

$$F_x = \mu_r P \qquad (2.20)$$

where μ_r is the dimensionless rolling coefficient [5]. The rolling friction coefficient often varies between 10^{-5} and 5×10^{-3}, while the static friction coefficient often varies between 0.1 and 1.

In these expressions, given by eq. (2.15),(2.16) and (2.20), the friction force is not dependent on any deformation that may occur when applying the normal force. That is why another, similar, expression for rolling friction can be useful to fully comprehend the mechanisms of friction. The expression can be derived from the equilibrium state of a cylinder exposed to a rotating torque, see figure 2.4.

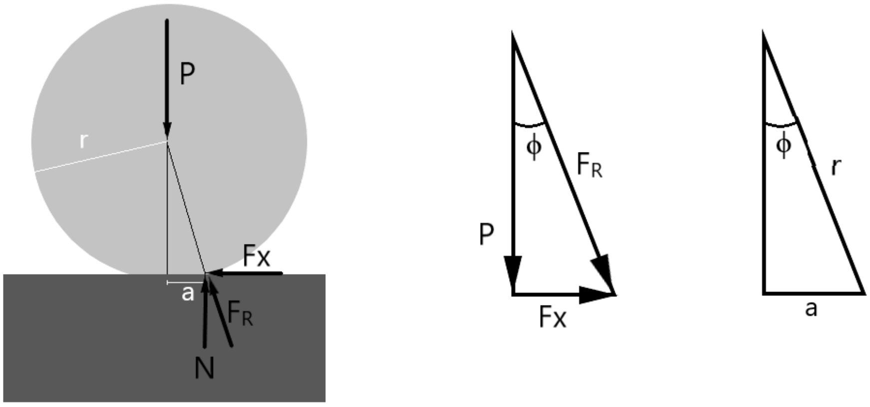

Figure 2.4: Illustration of a cylinder on a plane surface in equilibrium right before the cylinder starts rolling and the equilibrium forces and dimensions rearranged to equilibrium triangles.

The reaction force F_R, the normal force P and the friction force F_x can be rearranged as an equilibrium triangle, forming the same angle ϕ as the geometrical dimensions a, the half width of the deformed area, and the radius, r, of the cylinder, see figure 2.4. With trigonometry, and assuming that ϕ is small, an expression can be derived to provide

$$F_x = F_R \sin\phi \approx F_R\phi = \frac{F_R\phi r}{r} \approx \frac{F_R a}{r} \tag{2.21}$$

Using the Pythagorean theorem, the reaction force F_R can be written as $F_R = \sqrt{P^2 + F_x^2}$, subsequently inserted into eq. (2.21), which is then rearranged to provide

$$F_x = \frac{aP}{\sqrt{r^2 - a^2}} \tag{2.22}$$

This expression is of course similar to eq. (2.20), but it is easier to see the influence of deformation on the rolling friction.

The rolling friction coefficient can be determined experimentally in a corresponding way as the static coefficient of friction using eq. (2.19), see figure 2.3. Although, in the experiments performed as part of this Master's thesis project, finding the exact moment at which the object starts to roll demands much more precision and is a cumbersome method for evaluating the friction. In the case of, for example, a car tyre, where the deformation is rather large because of the more elastic material, it might be easier to determine the rolling friction. However, in the case of steel cylinders on a steel surface, as in the NCD friction drive, it is difficult to obtain valid results because of the near nonexistent deformation at the load levels under consideration in this Master's thesis.

2.2.1 Creep ratio

In the NCD friction drive, the interface between each component is exposed to a rolling contact between a cylinder and a plane surface. In the contact area, both a sliding domain and a sticking domain can exist [1]. The sliding cause a difference between the translational velocity, v, and the tangential velocity, ωR, which is the definition of *creep velocity.* The objective in most rolling contact applications is to minimise the absolute value of the creep velocity, letting a rolling body have the same translational and tangential velocity. Not only because of the energy loss that occurs when a rolling body starts to slide, but also because of the increase in wear of the contact surface that slide implies [1]. However, it is not theoretically possible for the two speeds to be exactly equal, due to deformations of the rolling body. Even if the deformations are purely elastic and very small, there will always be a difference between the velocities. The difference in velocity can also be expressed in terms of strains and the *creep ratio* can therefore, in its simplest form, be defined as

$$s = \frac{\epsilon_{xx}}{1+\epsilon_{xx}} \approx \epsilon_{xx} \tag{2.23}$$

Considering a cylinder with radius r, rolling on a plane body. Since Hertzian contact stress can be constructed by superposition, the tangential stress can then be divided into a two parts with different sliding and sticking behaviour. This scenario is illustrated in figure 2.5. Following [1] the total stress τ can be expressed as

$$\tau(x) = \tau_1(x) + \tau_2(x) \tag{2.24}$$

with

$$\tau^{(1)}(x) = \tau_1\Big(1 - \frac{x^2}{a^2}\Big)^{\frac{1}{2}} \tag{2.25}$$

$$\tau^{(2)}(x) = -\tau_2\Big(1 - \frac{(x-d)^2}{c^2}\Big)^{\frac{1}{2}} \tag{2.26}$$

The quiantities a, c and d are all half-widths of different regions of the contact area, see figure 2.5: a is the half width of the whole contact area, c is the half width of the sticking region and d is defined as $d = a - c$.

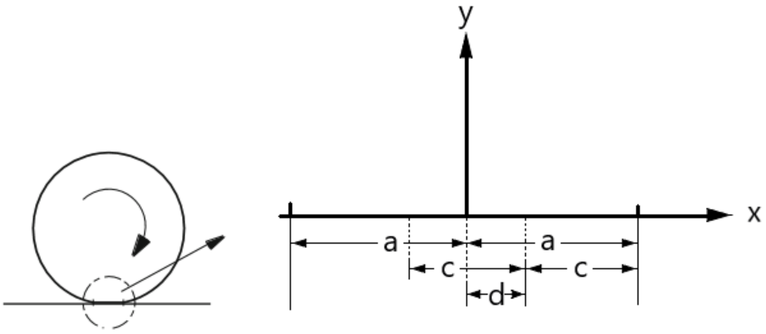

Figure 2.5: Description of the different regions in a rolling contact

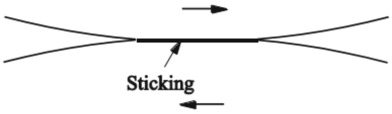

Figure 2.6: Illustration of two bodies in contact with tangential opposite forces

The derivation of the creep ratio starts with the relative displacement between two arbitrary bodies in contact. Both bodies have tangential loading forces in opposite directions, see figure 2.6, and according to [1] the displacement is written as

$$u_x = \frac{F_x}{2\pi G}\Big(\frac{1-v}{r} + \frac{vx^2}{r^3}\Big) \tag{2.27}$$

where v is the velocity, G is the shear modulus and $r^2 = x^2 + y^2$. Knowing that the stress varies inside the contact area, it is a good idea to express the displacement as a function of stress distribution instead. The tangential stress distribution between two spherical bodies in contact exposed to a tangential force is, according to [1], defined as

$$\tau(x, y) = \tau_0\Big(1 - \frac{x^2 + y^2}{a^2}\Big)^{-\frac{1}{2}} \tag{2.28}$$

To obtain the total displacement, this expression has to be integrated over the entire area, as in eq.(2.29). New variables are introduced with x' and y', being the coordinates in the new, deformed configuration while x and y are the coordinates in the undeformed configuration. $s^2 = (x - x')^2 + (y - y')^2$ is introduced as a help variable.

$$u_x = \frac{\tau_0}{2\pi G}\iint_A \Big(\frac{1-v}{s} + v\frac{(x-x')^2}{s^3}\Big)\Big(1 - \frac{x'^2 + y'^2}{a^2}\Big)^{-\frac{1}{2}} dx'dy' \tag{2.29}$$

According to [1], the integration over the area leads to

$$u_x = \frac{\pi(2-v)}{4G}\tau_0 a \tag{2.30}$$

which is a constant. This only applies to the more general case, where two spheres are in contact. If the two bodies in contact instead are a cylinder and a plane half space, the displacement for this case is obtained in a similar way and result in

$$u_x = const - \tau_0 \frac{x^2}{aE_{eff}} \tag{2.31}$$

where E_{eff} is the effective Young's modulus, defined in eq. (2.1). Applying the super position principle from (2.24)-(2.26) together with the definition of the different regions in the contact area lead to the total displacement of

$$u_x = const - \tau_1 \frac{x^2}{aE_{eff}} + \tau_2 \frac{(x-d)^2}{cE_{eff}} \tag{2.32}$$

This formulation is then used to define the strain as

$$\epsilon_{xx} = \frac{\partial u_x}{\partial x} = -\tau_1 \frac{2x}{aE_{eff}} + \tau_2 \frac{2(x-d)}{cE_{eff}} \tag{2.33}$$

This expression has to fulfil the requirement that in the sticking domain, the deformation is constant [1]. This means that the deformation should be equal if $x = d$ or $x = c$, for example. Both are in the sticking region, see figure 2.5. This leads to the relation between τ_1 and τ_2 being

$$\frac{\partial u_x}{\partial x}|_{x=d} = \frac{\partial u_x}{\partial x}|_{x=c} \Longrightarrow -\tau_1 \frac{2c}{aE_{eff}} + \tau_2 \frac{2(c-d)}{cE_{eff}} \Longleftrightarrow \tau_2 = \tau_1 \frac{c}{a} \tag{2.34}$$

In the sliding domain, Coulomb's law, $F_x = \mu_s P$ has to be valid. Since the location of the highest shear stress due to sliding, τ_1, is at the same location as the highest Hertzian pressure, p_{max}, it must hold that

$$\tau_1 = \mu_s p_{max} \tag{2.35}$$

With eq. (2.34) and (2.35), the constant part of the deformation, the sticking region, can be fully defined as

$$\frac{\partial u_x}{\partial x}|_{stick} = -\frac{2\mu_s p_{max} d}{aE_{eff}} \tag{2.36}$$

With τ_1 and τ_2 defined, the total shear stress expression can be fully defined as well. With the findings in eq. (2.34) and (2.35) and with the expressions in eq. (2.24)-(2.26), the total shear stress is

$$\tau(x) = \mu_s p_{max}\Big(1 - \frac{x^2}{a^2}\Big)^{\frac{1}{2}} - \frac{c}{a}\mu_s p_{max}\Big(1 - \frac{(x-d)^2}{c^2}\Big)^{\frac{1}{2}} \tag{2.37}$$

To obtain the total force in the x-direction this expression has to be integrated over the whole contact area, between $-a$ and a. The latter step provides

$$\begin{aligned} F_x &= L\int_{-a}^{a}\tau(x) = L\mu_s p_{max}\int_{-a}^{a}\Big(1-\frac{x^2}{a^2}\Big)^{\frac{1}{2}} - \frac{c}{a}\Big(1-\frac{(x-d)^2}{c^2}\Big)^{\frac{1}{2}}dx \\ &= L\mu_s p_{max}\left[\frac{a\,sin^{-1}(\frac{x}{a})}{2}+\frac{x\sqrt{1-\frac{x^2}{a^2}}}{2}-\frac{c^2}{a}\frac{sin^{-1}(\frac{x-d}{c})}{2}+\frac{(x-d)\sqrt{1-\frac{(x-d)^2}{c^2}}}{2}\right]_{-a}^{a} \\ \Longleftrightarrow F_x &= \frac{L\mu_s p_{max}\pi a}{2}\Big(1-\frac{c^2}{a^2}\Big) \end{aligned} \tag{2.38}$$

By using the definition of the Hertzian pressure for a cylinder and a plane, eq. (2.11), the expression can be rewritten as

$$F_x = \mu_s P\Big(1-\frac{c^2}{a^2}\Big) \tag{2.39}$$

and with the help of the definition of d as $d = a - c$, the expression can be rewritten as

$$\frac{d}{a} = 1-\Big(1-\frac{F_x}{\mu_s P}\Big)^{\frac{1}{2}} \tag{2.40}$$

which comes in handy when formulating the final expression for the creep ratio. As previously mentioned, the creep ratio can be approximated as the strain, ϵ_{xx}, in the rolling direction, which is the same as the strain found in eq. (2.36). By inserting eq. (2.40) in eq. (2.36) the creep ratio can be written as

$$s = -\frac{2\mu_s p_{max}}{E_{eff}}\left(1-\sqrt{1-\frac{F_x}{\mu_s P}}\right) \tag{2.41}$$

or, with $P = \frac{\pi E_{eff} L a^2}{4R}$, which comes from an approximation of how the force depends on the penetration depth [1], and with the definition of Hertzian contact pressure eq. (2.11) the creep ratio can also be expressed as

$$s = -\frac{\mu_s a}{R}\left(1-\sqrt{1-\frac{F_x}{\mu_s P}}\right) \tag{2.42}$$

According to [1], the creep ratio for three-dimensional bodies can be derived in a similar way and result in

$$s = -\frac{(4-3\nu)\mu_s a}{4(1-\nu)R}\left(1-\Big(1-\frac{F_x}{\mu_s P}\Big)^{\frac{1}{3}}\right) \tag{2.43}$$

Evaluating the expression for the two dimensional creep ratio in eq. (2.42) it can be seen that

$$\frac{F_x}{\mu_s P} \leq 1 \tag{2.44}$$

must be fulfilled for the expression to be valid. If eq. (2.44) is not fulfilled, then the bodies have not entered the stick- and slip region but only the slip region, where the expression is not applicable. It's a very logical limitation which yield the same result as Coulomb's static friction in eq. (2.15).

2.3 Fatigue

One of the most severe possible issues with the NCD friction drive is not deformations due to the static load, but deformations due to repeated loads as the door opens and closes. ASSA ABLOY has identified this type of cyclic deformation, causing material fatigue, as a critical problem.

The whole fatigue process can be divided into five main stages [6]. The first stage starts when changes appears in the microstructures. The location of these changes becomes the origin of the permanent damages. The second stage is creation of cracks on the microscale, also called crack initiation. In the third stage the microscopic cracks grows and eventually some of the cracks might link together. These are called *dominant cracks* and they are the critical cracks that eventually will lead to failure. This stage is usually considered to be the beginning of crack propagation. In the fourth stage the propagation of the cracks continues in a stable way. In the fifth stage the propagation is no longer stable and leads to fracture [6]. A simplified scheme of the fatigue process is shown in figure 2.7.

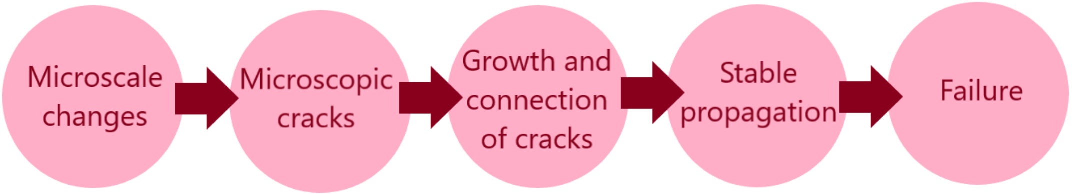

Figure 2.7: The five key stages of a fatigue failure.

There are two main approaches to fatigue life models, *Total-life* approach and *Defect-tolerant* approach [6]. In the total-life approach the total fatigue life is considered. This means that the total number of load cycles that are required to initiate a crack plus the total number of cycles that are required to reach a critical size of the crack are included. The defect-tolerant approach assumes that all components have flaws from the start. The life is therefore calculated as the number of cycles required for an already existing crack to grow to a size where failure occurs. The initiation stage is not considered at all in this approach [6]. Since there is no experimental setup available for evaluating the existing flaws in the NCD friction drive prior to the cyclic loading, the defect-tolerant approach is difficult to use in this Master's thesis. Instead, the fatigue model is based on the total-life approach. In the total-life approach, the life can be presented with an S-N curve, which has the number of cycles to failure on the horizontal axis and stress amplitude on the vertical axis, see figure 2.8.

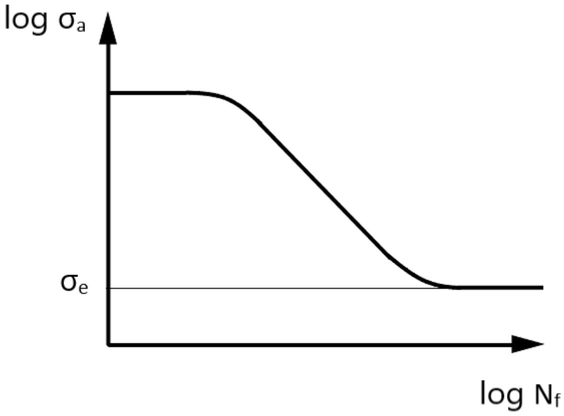

Figure 2.8: Illustration of how a basic, general S-N curve can look like.

Some important definitions of different stress expressions used in fatigue life calculations are presented below.

- Endurance limit, σ_e, is the stress amplitude below which the material or structure will have infinite fatigue life, see figure 2.8. The endurance limit is usually between 35% and 50% of the tensile strength for steel alloys [6]. Some alloys do not exhibit an endurance limit. Then, the S-N curve does not flat out, but continue to decrease. In these cases the endurance limit can be approximated as the stress amplitude the sample or component can endure for 10^7 cycles.
- The stress range is defined as $\Delta\sigma = \sigma_{max} - \sigma_{min}$
- The stress amplitude is defined as $\sigma_a = \frac{\sigma_{max} - \sigma_{min}}{2}$
- The mean stress is defined as $\sigma_m = \frac{\sigma_{max} + \sigma_{min}}{2}$
- The load ratio is defined as $R^* = \frac{\sigma_{min}}{\sigma_{max}}$

It can sometimes be effective to use a model for fixed life. In these cases, an expression for calculating the the maximum allowed stress amplitude that a material can be exposed to and still have a theoretical infinite life is used. Three of the most common expressions for fixed life are presented in table 2.1 together with some pros and cons for each expression.

Table 2.1: Three different expressions for calculating stress amplitude.

Name	Expression	Application and limitations
Soderberg	$\sigma_a = \sigma_a\|_{\sigma_m=0}\left(1 - \frac{\sigma_m}{\sigma_Y}\right)$	Using this expression will give a conservative result for most engineering alloys.
Gerber	$\sigma_a = \sigma_a\|_{\sigma_m=0}\left(1 - \left(\frac{\sigma_m}{\sigma_{TS}}\right)^2\right)$	This expression does not make any difference between compressive and tensile mean stresses. It is most suitable to use on tensile stresses and gives good approximations for ductile alloys.
Modified Goodman	$\sigma_a = \sigma_a\|_{\sigma_m=0}\left(1 - \frac{\sigma_m}{\sigma_{TS}}\right)$	This expression gives a good approximation for brittle materials and give conservative results for more ductile alloys. It does however lead to overestimations of the fatigue life for compressional stresses.

σ_Y is the yield strength and σ_{TS} is the tensile strength [6]. $\sigma_a|_{\sigma_m=0}$ is the stress magnitude when $\sigma_m = 0$ and R^*=-1, which is the same definitions as the endurance limit σ_e.

Based on these descriptions it becomes clear that Soderberg's expression is the most suitable for calculating the maximum allowed stress amplitude for the NCD friction drive. Both the Gerber expression and the modified Goodman are unsuitable for compressional mean stresses, which is the dominating type of stress in the NCD friction drive.

When calculating the fatigue life, some fatigue life models are only defined for a mean stress of zero, for example the Basquin model [6]

$$\sigma_a = \sigma'_f(2N_f)^b \tag{2.45}$$

where σ'_f is the fatigue strength coefficient, N_f is the number of cycles to failure and b is the fatigue strength exponent. This model is not applicable to the NCD friction drive since the mean stress is non-zero. The number of cycles to failure can instead be calculated with Morrow's relation. It is a modification of the Basquin expression and is defined as

$$N_f = \frac{1}{2}\left(\frac{\sigma_a}{\sigma'_f - \sigma_m}\right)^{\frac{1}{b}} \tag{2.46}$$

However, the fatigue process is slightly different for contact fatigue and especially rolling contact fatigue. That is why the model for calculating regular fatigue life has to be used as a complement to other models, more suitable for contact fatigue.

Repetitive rolling contact can for example, in the early cycles, lead to residual stresses that can mitigate the effect of the applied loads and lead to less plastic deformations even though the applied load would imply higher stresses than the yield condition allows [6]. This can only occur if the applied load is below a certain value, called shakedown limit. If the load exceeds the shakedown limit, then the plastic strains will accumulate and the structure will eventually collapse. The accumulation of plastic strains during cyclic contact loading is called ratcheting. The concept is similar to the fatigue previously described, but instead of formations of cracks, the eventual failure is based on an accumulation of plastic strains produced during each cycle [6]. The locations of the ratcheting depends on the surface roughness and is often divided into to categories depending on the coefficient of friction. If $\mu_s < 0.3$ the ratcheting wear occurs on the surface, while if $\mu_s > 0.3$ the wear occurs just below the surface [6].

The shakedown limit for tractive rolling of a cylinder can behave slightly different depending on if the yielding of the material occurs on the surface or under the surface. It is therefore easiest to evaluate the shakedown using the diagram presented in Appendix A, figure 8.1. If the stress ratio p_{max}/k is above the curve, the shakedown limit is exceeded and the component will gradually wear until collapse. If it is under the shakedown limit, the component is assumed to have infinite ratcheting life. k is defined as

$$k = \frac{\sigma_Y}{\sqrt{3}} \tag{2.47}$$

where σ_Y is the yield strength of the material.

The stages of contact fatigue are basically the same as the general stages, see figure 2.7. But the macro cracks that are formed during the stable propagation corresponds to spalling on the surface [7]. A spall is a crater that is created in the contact surface due to repetitive rolling contact. Spalling is also referred to as pitting.

In the first phase of contact fatigue, where initial changes of the material properties occurs, both the hardness and the surface roughness can change [7]. The surface roughness usually decrease because of the wear, whereby the asperities are reduced and the surface becomes increasingly polished. In the ideal application, the fatigue process would stay within this stage and never reach the final stage, where the spalling occurs.

Rolling contact fatigue can often be divided into low or high cycle fatigue and ratcheting fatigue [8]. The exact number of cycles that separates low- and high cycle fatigue is not defined. High cycle fatigue, HCF, is defined as fatigue that occurs when low stress amplitudes induces elastic deformations [6]. Low cycle fatigue, LCF, is defined as fatigue that occurs when the stress amplitude is high and plastic deformation occurs. The number of cycles to failure is lower in this case, hence the name.

In the NCD friction drive the dominant type of fatigue, except for ratcheting, is most likely LCF. The components show plastic deformations after being in the test rig for a while and ASSA ABLOY predicts that deformations can be visible after just a short time when it comes to the basic material setup already used. It is difficult to predict which kind of fatigue that will lead to failure for the material. That is why it is crucial to calculate both the low cycle fatigue life and the ratcheting life and then compare them. In this master thesis, the LCF will be calculated with Morrow's relation, eq. (2.46).

Calculating the ratcheting fatigue life can be done with the expression

$$N_f = \frac{\epsilon_c}{\sqrt{(\Delta\tilde{\epsilon})^2 + (\Delta\tilde{\gamma}/\sqrt{3})^2}} \tag{2.48}$$

where ϵ_c is a material constant. The constant can only be obtained from experiments, which brings a certain difficulty to the model [8]. $\Delta\tilde{\epsilon}$ is the average ratcheting axial strain range and $\Delta\tilde{\gamma}$ is the average ratcheting shear strain range. These two are obtained from the Ansys simulations, using the result on the plane with the largest range of shear strain.

Of course, it is not only the applied force and the resulting stress that affects the fatigue life. Other factors, such as the surface roughness and hardness can also play a large part in how many cycles a material or structure can withstand before failure.

2.3.1 Influence of surface roughness on fatigue life

When two bodies are brought into contact, the real contact does not exist across the whole apparent contact area, but at several individual smaller areas, see figure 2.9. This means that the Hertzian contact pressure, as well as the friction, depend on the surface roughness.

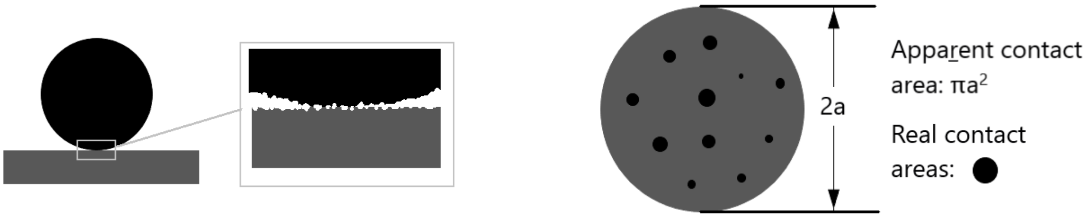

(a) Rough surface contact

(b) Contact areas

Figure 2.9: Illustration of how the surface roughness influence the contact in the form of contact points and the difference between apparent contact and real contact.

Surface roughness is rarely constant in a dynamic system. The wear that appears during cyclic load often leads to a reduced surface roughness [3]. This change in surface roughness can also alter the size of the contact surface between two bodies, and therefore also change the Hertzian contact pressure. It can also change the coefficient of friction slightly.

According to [9], for low cycle fatigue, the influence of surface roughness can be approximated with the expression

$$N_f = C_{spec} R_a^{-0.1166} \tag{2.49}$$

This expression is purely experimental and was obtained using a steel alloy with a yield strength of 420 MPa. N_f is the number of cycles to failure, C_{spec} is a constant that depend on the geometry and load, R_a is the arithmetical mean deviation of the surface. And as previously mentioned, it is only valid for low cycle fatigue and only for surface roughness R_a between approximately 0.1 μm and 1.7 μm, assuming that it can be applied to other similar steel materials. Most engineering structures made of steel has a surface roughness between approximately 0.2 μm and 1.6 μm [9].

2.3.2 Influence of hardness on fatigue life

Hardness is usually measured using a tool that is used to make an indentation on the surface. The ratio between the applied load and the surface of the indention or the projected area of the indentation is then calculated. The exact definition differs between different tests, where different indenter geometries are used [10]. The earliest developed modern hardness test was the Brinell test, where a steel ball was used as an indenter. Later, other types of tests with a range of different geometries were developed by for example Vickers and Rockwell. The translation between the different measurements can be done with a table, for example the *Bodycote conversion table* [11]. Following [10], the relationship between hardness and yield strength is often approximated as

$$HV \approx 3\sigma_Y \tag{2.50}$$

However, in reality the ratio of hardness to yield strength has a more complex relationship than this. Young's modulus, indenter geometry, Poisson's ratio and other factors can affect the value as well [10]. It is appealing to use the very simple relationship presented in eq. (2.50), however it is important to understand that the precision of the relationship is different for different materials. For example, the relation should only be applied on materials that have not been exposed to work hardening. It is also quite easy to imagine that metals that have been subject to a surface treatment to increase surface hardness, do not follow the relation of $HV \approx 3\sigma_Y$. This assumption was merely based on the fact that several material and hardness treatments described in the *Bodycote heat guide* does not match this relation [11]. Other relations were found for these special cases.

For three different metals, the relation between hardness and yield strength is linear up until a certain point [12]. For some of the metals the yield strength increase up to a hardness of approximately 700 HV, where the yield strength either increased with a flatter slope or decreased, while other continued to increase linearly. The pattern for three different steel alloys was that for each 1 HV that the hardness increased, both the tensile strength and yield strength increased with an approximate factor of 3.5. In other words, the parameters followed the expression $\sigma_Y = \sigma_{Y0} + 3.5\Delta HV$, where σ_{Y0}

is the yield strength without surface treatment. Assuming that this applies to similar metals, a component with a yield strength of 600 MPa and hardness of 300 HV would get a yield strength of approximately 2700 MPa when the hardness is increased to 1000 HV. This is a very high yield strength, that appears almost unrealistic. That is why this relation might not be the most appropriate model to use for predicting the change of yield strength when the surface hardness is increased. It could be that the hardness is so high that the yield strength relation has exceeded the linear region and dropped down to a much lower value, which means that the hardness of choice should be reduced to obtain a more satisfactory yield strength. Or it could be that this relation is not applicable for the specific range of hardness or the material used in this Master's thesis.

Another relation between hardness and yield strength is obtained from [13]. The hardness and yield strength, both normalized with Young's modulus, follow the relation in eq. (2.51) rather closely when Poisson's ratio, $\nu = 0.3$. This expression would mean that with a Young's modulus of 200 GPa and a hardness of 1000 HV, the yield strength would be 200 MPa. This is a very low value that also seems unreasonable. The problem can be that the relation is developed using materials such as copper- and aluminium alloys, while the NCD friction drive is made of different types of steel. Regardless the reason, there are two different expressions to determine the yield strength when the hardness is increased. One overestimates and one underestimates the yield strength. This shows how difficult it is to find a general model that is applicable for a large range of commercially available materials.

$$\frac{HV}{E} = \frac{1}{2}\left(\frac{\sigma_Y}{E}\right)^{\frac{2}{3}} \tag{2.51}$$

In reference [14] the steel SS 2940, with composition 41CrAlMo7, has a yield strength of 1251 MPa when the hardness is 1281 HV. This is after the metal has been quenched, tempered and gone trough a nitriding treatment. The material, prior to all treatments, have a yield strength of approximately 600 MPa and a hardness of 290 HV [15]. The hardness is converted with the conversion table in [11]. In rough approximations, the yield strength and hardness relation can be described by the expression

$$\sigma_Y = \frac{1}{2}\sigma_{Y0}\frac{HV}{HV_0} \tag{2.52}$$

Where σ_{Y0} and HV_0 are the yield strength and hardness of the material without surface treatment. σ_Y and HV are the yield strength and hardness after the material has been subject to the surface treatment. It is not proven that this relation is applicable to all metals, but in this Master's thesis this relation is considered the most appropriate alternative to relate the hardness to the yield strength. It is also assumed that the endurance limit, σ_e, and the fatigue strength coefficient, σ'_f, follows the same relation.

3 Previous Work

3.1 Previous Test Setup

ASSA ABLOY had already done some practical tests on the NCD friction drive before this Master's thesis project started. The tests were done in a testing rig, similar to the intended design but with some simplifications.

The test rig used for earlier tests was created with components that ASSA ABLOY had to spare in the workshop. Therefore it did not have the correct dimensions and the material was an ordinary steel without any surface treatment. The bearings that should be placed on both sides of the rods have, as mentioned earlier, high requirements on a small diameter to not exceed the total height limit of the unit. However, in the test rig the bearings were almost four times bigger than they can be in the final design of the NCD friction drive.

In the test rig design, the bearings were placed on a shaft and both the upper and the lower bearing was in contact with the respective rod, see figure 3.1a. This worked because the inner diameter was large, but in the final design this would imply that the bearing shaft would be just a few millimetres in diameter and would therefore be too thin to endure the high stresses without cracking or bending. This assumption is not calculated or simulated, but merely taken from the advise of experienced designers at ASSA ABLOY.

The solution for this problem would be to, instead of having a shaft fixed in support plates on both sides and with one or more bearings, use the reversed design. In other words, use a shaft which has two bearings on each side, which are fixed in the support plates, see figure 3.1b. This means that it is the shafts that have contact with the rods, instead of the bearings.

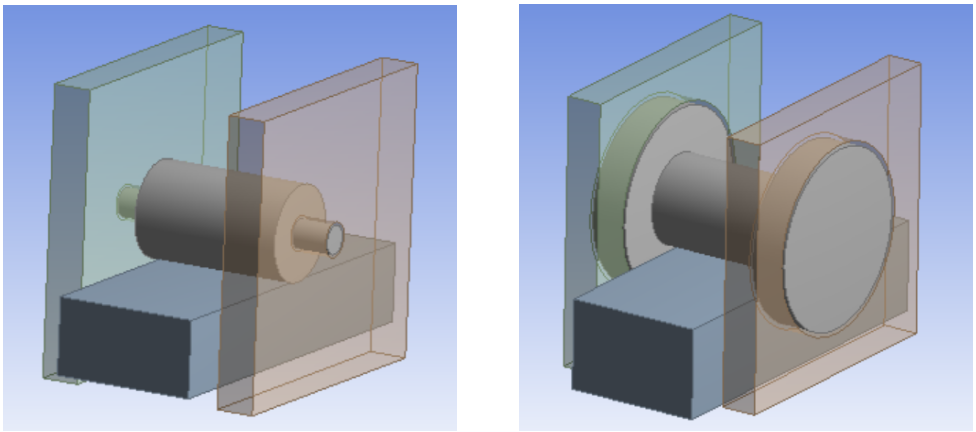

(a) Previous setup

(b) Desirable setup

Figure 3.1: Illustration of how the bearing and bearing shaft previously was designed for the test rig and the suggestion of the final setup for the NCD friction drive bearing shafts.

Designing and manufacturing a new test rig with these changes would take a long time and not leave much time for performing actual tests, which is why the basic setup was the same in the new tests. This means that the results from the practical tests on the bearings and the bearing side of the rods are not of interest. The main focus will be on observing the driving shaft and the contact surface counterpart on the rods. In the final design, the bearing shaft will most likely have a similar diameter and width as the driving shaft, which is why the observations on the driving shaft contact surfaces from the practical tests can be applicable, in some extent, for the bearing shaft as well.

3.2 Previous Test Results

The previous tests done in the test rig point to a number of problems with the materials and dimensions. The rods, that are supposed to be driven back and forth, exhibit distinct wear patterns. Figure 3.2b shows the rod surface at the turning point for the surface in contact with the driving shaft. The right half of the rod shown has not been exposed to cyclic loading. Again, the contact surface for the bearing shaft side is not applicable to what the final result may look like, but it can be used for comparisons with the other side of the rod, see figure 3.2. The driving shaft side of the rods exhibit wear in a striped pattern and at the turning point, where the driving shaft may have experienced a large amount of slip, there is a distinct cavity in the material. The driving shaft exhibits a similar appearance, which can be seen in figure 3.3. The whole circumference is covered with a striped wear pattern.

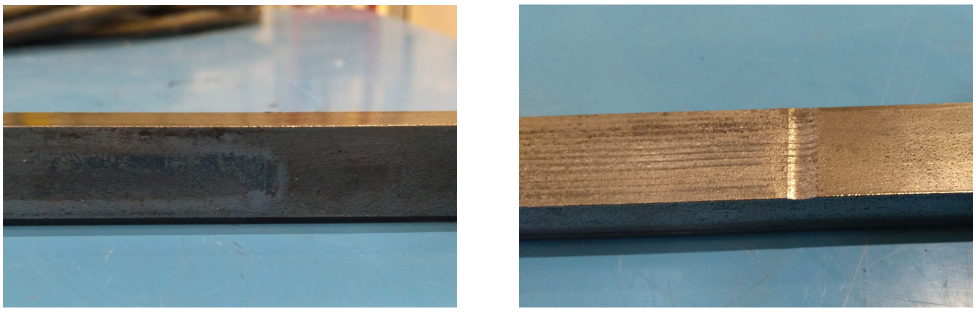

(a) Rod on bearing side

(b) Rod on driving shaft side

Figure 3.2: Image of wear patterns on the rods resulting from cyclic loading in the test rig.

Figure 3.3: Image of wear patterns on the driving shaft resulting from cyclic loading in the test rig.

This indicates that there are problems with the material and the design used in the previous test setup. The wear on the surface and the deformation in the material can be prevented if the material has a higher hardness, but there may also be some other design issues that comes from misalignment of the components, for example.

3.3 New Test Setup

The choice of material for the new test setup was based on both theory and recommendations from an external company, Bodycote, who specialise in surface treatments for different materials. Figure 3.2 and 3.3 show results from previous tests, where the surface exhibit severe deformations. The objective is to minimise these deformations such that they do not affect the performance or safety of the NCD.

In section 2.3.2 the relation between hardness and fatigue was discussed. It is shown that increased hardness has a positive effect on the yield strength and therefore also the life span. That is why the new test material should have higher hardness to avoid deformations. It is also important to keep in mind the difference in number of cycles each component is exposed to. The rods will be exposed to one loading cycle at each point of the rod's length per opening or closing. The shafts, however, will rotate and be exposed to load variations much more frequently. During one full revolution of the driving shaft, each point on the circumferential will be exposed to high stresses twice. Hertzian contact pressure is applied on both sides of the driving shaft because of the two rods. The bearing shafts will be exposed to high stresses once per revolution.

With this in mind, the requirements on fatigue resistance is higher for the shafts than the rods.

Even though the stresses mainly exist on the surface, it might not be enough to use an arbitrary material with a surface hardness treatment. The surface hardness and the depth of the hardness treatments can vary depending on the composition of the material, according to Bodycote [11]. For example, with the treatment type *gas nitriding*, a low alloy steel will get a larger diffusion zone, which can be used as a measurement of how deep into the material the hardness is affected. It will however yield a lower surface hardness. A high alloy steel will get a smaller diffusion zone, but the surface hardness will be higher.

After describing the problem of the NCD friction drive for a representative from Bodycote, they recommended materials and surface treatments that were used in the first version of the test rig:

- Shafts: tempered steel SS 2541 with the heat treatment Corr-i-Dur.
- Rods: Arbitrary steel with heat treatment Corr-i-Dur.

Corr-i-dur is a thermochemical treatment [16]. It can improve wear resistance, fatigue life and surface hardness. At the same time, it creates a resistance to corrosion. The corrosion protection was not a requirement at this point of the product development process, but the more experienced designers at ASSA ABLOY thought it was a good idea, because corrosion has previously been a problem in certain environments for similar night closing doors. The recommendations from Bodycote were used in one of the new test setups. The arbitrary steel in the rods was chosen to be the same as in the rods, SS 2541.

The second test setup was decided, not from recommendations, but from curiosity about how an extreme value would affect the NCD friction drive unit. Tempered nitrate steel SS 2940-03 can, according to Bodycote, get a surface hardness up to 1100 HV with the surface treatment *gas nitriding* [11]. From a practical experiment point of view it is interesting to see how the surface behaves during cyclic loading for such a hard material and surface. It might not be the material and surface treatment that is the most profitable for the final design, but it can give indications about if the hardness is one of the more critical factors, or if other parameters are more important. In other words, if the wear behaviour is not significantly improved by the extreme surface hardness, then the problem lies to a greater extent in, for example, applied compression force, surface roughness and so on.

The material and surface treatment for the rods in the second version of the test rig was:

- Shafts: Tempered steel SS 2940-03 with the surface treatment gas nitrating
- Rods: SS Tempered steel SS 2940-03 with the surface treatment gas nitrating.

The plan was to perform tests with two sets of material- and surface treatment combinations parallel in two different test rigs and let the fatigue testing go on for approximately four weeks. However, due to Covid-19, the second test rig, which was supposed to be produced by the ASSA ABLOY workshop in China, never arrived to Sweden. Also due to Covid-19, the testing components of the different material combinations were delayed. This lead to that the testing process had to be shortened significantly to get results on time. Only one of the material combinations were tested and the fatigue test only ran during approximately one week. The surface of the testing components were also supposed to be analysed thoroughly by an external company to draw conclusions of how the surface was affected by cyclic loading. However, because of the time limitation the surfaces had to be analysed by a nearby workshop with the tools available there. This meant that the precision of the result was not as good as planned. Despite this, it is possible to draw conclusions from the result.

4 Models and Calculations

The main focus of the theoretical model for the dynamic system is to include all relevant parameters to minimise the sliding friction and rolling resistance and at the same time minimise the stresses in all components. The theoretical model for the fatigue calculations focus on maximising the life and minimising the wear.

4.1 Geometric Dimensions

Increasing the length, L, of the contact area or the radius, R, of the cylindrical shafts both lead to a creep ratio closer to zero, but in different rates. Figure 4.1 shows that starting with the same radius and length and then increasing the respective dimensions separately, changing the length is more effective when optimising the creep ratio than if the radius is increased the same amount.

It is evident that the best choice to avoid high slip is is a large contact surface. The optimal choice of dimensions, is therefore the maximum allowed radius and length of the shaft. But is it possible to find dimensions that are smaller than the maximum and that still yield a sufficient creep ratio? If, for example, the creep ratio only decreases by 5% when the radius for example increase from 5 mm to 5.5 mm, it might be worth the extra slippage to make the NCD friction drive shaft smaller at the expense of other dimensions of the unit.

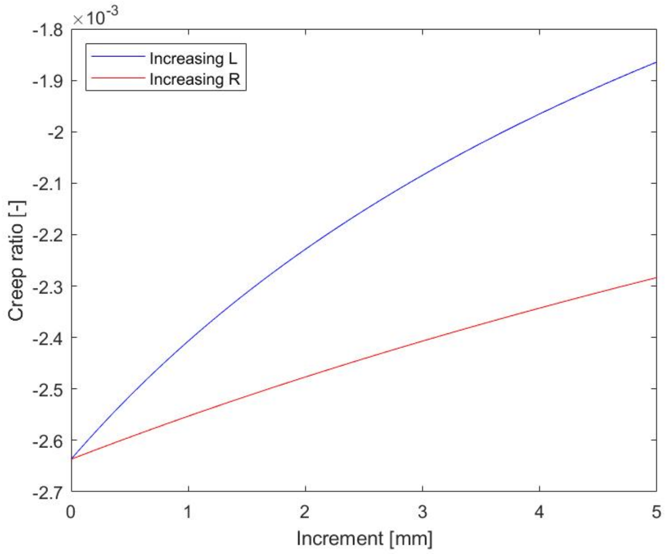

Figure 4.1: Plot illustrating how the dimensions affect the creep. Blue plot represent the creep as the length is increased from the original dimensions and the red plot represent the creep as the radius of the cylinder is increased from the same original dimensions. The plots are genereated with eq. (2.9) and (2.42).

The dimensions of the components in the NCD friction drive was calculated to both fulfil the requirement of minimising the Hertzian contact pressure and to obtain creep ratio close to zero, see section 2.1 and 2.2. As earlier mentioned, both the driving shaft and the bearing shafts can be viewed as cylinders in contact with a plane half space when calculating the contact pressure. With eq. (2.11) the contact pressure is plotted as a function of applied compression force, P, for different combinations of radius and length, see figure 4.2. For these calculations E = 200 GPa and $\nu = 0.3$ for both bodies.

The calculations were also used to plot the relation between the applied compression force and the creep ratio for different combinations of radius and length to get a better understanding of how the slip and stick relation depends on geometric dimensions, as shown in figure 4.3. The friction coefficient is $\mu_s = 0.2$ and the frictional force is set to $F_x = 150N$. It is not surprising that the cylinder with the largest radius and length provided the best creep ratio (closest to zero), since this also implies the largest contact area. However, it is interesting to see that the creep ratio in the plot was approximately the same for L=25 mm, R=6 mm and L=30 mm, R=5 mm. Same applies to L=20 mm, R=6 mm and L=30 mm, R=4 mm. This implies that it is possible to obtain the same creep ratio for a longer cylindrical shaft with a smaller radius as for a shorter cylindric shaft with a larger radius. The same applies to the contact pressure. The same behaviour was seen in figure 4.1, but now put in the context of actual dimensions. Since the height of the NCD friction drive unit is more critical than the width/depth it is an easy conclusion to draw, that the friction drive shafts should be as long as possible while keeping the radius smaller.

Even though the creep ratio is important to optimize the NCD friction drive, the difference between the highest and the lowest ratio in figure 4.3 is rather small. In practice, the NCD friction drive will be approximately equally effective if the creep ratio is -0.002 as if it was -0.0008 because both indicate that the sticking region is significantly dominant. That is why the creep ratio will be of less importance in this Master's thesis and more focus will be put on ensuring that the NCD friction drive is in the sticking region. The dimensions in the simulation model and in the practical tests will instead be determined based on previous test results and on ASSA ABLOY's predictions of how the final design will be.

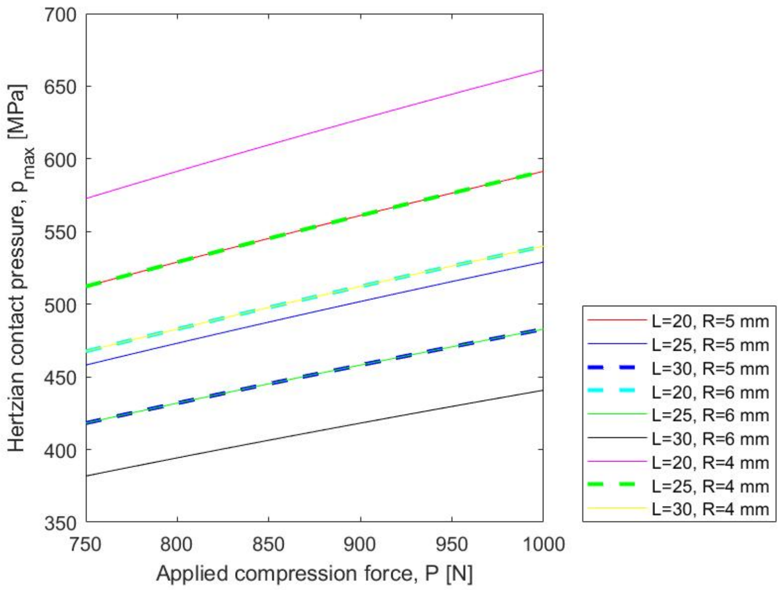

Figure 4.2: Maximum contact pressure as a function of applied force for nine different cylinder dimension combinations.

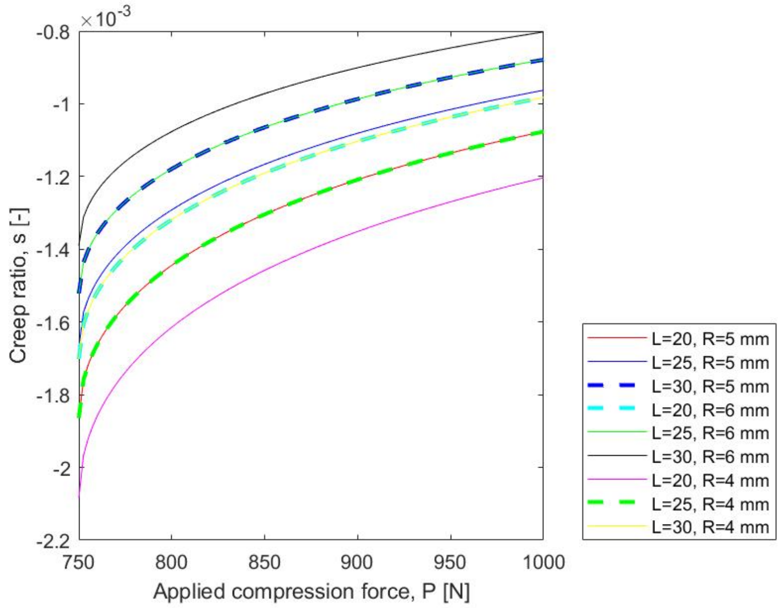

Figure 4.3: Creep ratio as a function of applied force for nine different cylinder dimension combinations.

The rods that were used in the previous test setup had a thickness of 10 mm and a width of 15 mm. Again, this was mainly because the first version of the test setup was made with materials and components that were easily accessible in the workshop. In the final version, ASSA ABLOY would like the rod to be 8 mm thick instead, so that the total height is reduced further. The width of the rod could in theory be as wide as 30 mm in the final version. However, ASSA ABLOY expressed interest in keeping the width of the rod to 15 mm if possible, only increasing the width if the results point to a much too fragile system.

If the maximum height of the whole unit is 54 mm and the rods are allowed to be as thin as 8 mm, the driving shaft and the bearing shafts are allowed to have a diameter of 12 mm, with 2 mm still to spare

$$h_{total} = 2 \times D_{bs} + 2 \times t_r + D_{ds} = 2 \times 12 + 2 \times 8 + 12 = 52 \text{ mm} \tag{4.1}$$

However, the device that is used at present to compress the components is placed around the unit and take up some space above and beneath the components. If the compression device cannot be designed to avoid a greater height than the total of the three shafts and two rods, the shaft diameters cannot be 12 mm. Since the construction and design of the complete NCD friction drive unit, including the compression device, is outside of the scope of this Master's thesis, it is deemed to be a good idea to keep using the 10 mm diameters on all cylindrical shafts for the future calculations and simulations. That way, the results are related to ”the worst case scenario”. If the compression device in the future can be designed to not take up any space over and under the NCD friction drive components, then dimensions of the components can be increased slightly, which will only improve the results.

In practice, the three shafts will probably be slightly longer than the rods are wide so that the rods can easily be rolled back and forth. This is why, in the Ansys model, the shafts are 16 mm long while the rods are 15 mm wide. All dimensions used in the subsequent simulations and calculations in this Master's thesis are presented in figure 4.4. In reality, the rods are several meters long, which is why they are shortened in the illustration.

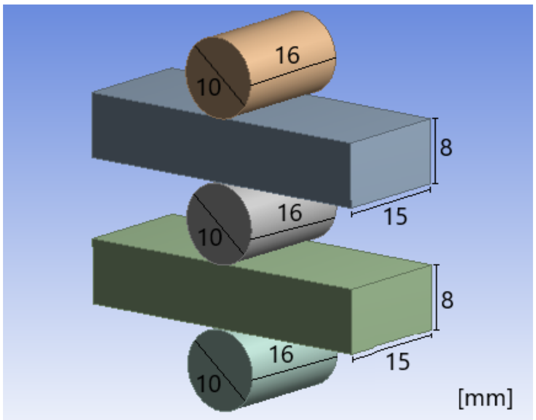

Figure 4.4: The dimensions of the components of the NCD friction drive unit for future calculations, simulations and tests.

4.2 Forces and Coefficient of Friction

As described in section 2.2, it is difficult to determine the rolling friction coefficient by experimental methods with the material combination steel-steel, since the deformation is very small and no tools with high enough precision were available to record the angle at which rolling occurs. That is why the static sliding friction, μ_s was determined instead. This is also a suitable method to use, since it is the static coeffificient of friction that is later used in the numerical Ansys model.

A plot was created to show the relation between the friction coefficient and the compression force needed to obtain a friction force of 150 N, using Ansys Workbench, see figure 4.7. The reason for not using the expression for Coloumb's friction eq. (2.15) directly was that the basic equation only applies to a setup with one contact surface, while the NCD friction drive has two. The theory was that the resistance in rolling could be greater with two contact surfaces. Also, as mentioned in section 2.2, rolling contact always contains both a sticking and a sliding region, which makes the expression for static friction, eq. (2.15), not completely accurate for calculating the required normal force in rolling friction. It can however be used as a good estimate.

When the material for the new test rig arrived, the friction coefficient could be calculated with the experimental method described in section 2.2 and be used for verification of the model.

4.2.1 Ansys model

The model for simulating the rolling of the NCD friction drive was built as a 2D model with two rods, in the form of rectangles, and three circles representing the two supporting bearing shafts and the driving shaft. Both the bearing shafts and the driving shaft had inner cylinders placed as concentric circles with smaller radii inside the shafts. This does not represent any geometric shape in the real friction drive, but is merely a way to place boundary conditions and forces on areas that do not interfere with the crucial contact area, since this lead to convergence problems otherwise. This particular model was created to either have movable rods, when the stresses and strains during friction drive was to be studied, and to have locked rods when the reaction forces was to be studied. The complete model with mesh is presented in figure 4.5. The elements are all quadratic and the integration order is linear for the whole mesh. Note that the coordinate system is different from how it was defined in figure 2.2. The new coordinate system can be seen in figure 4.6.

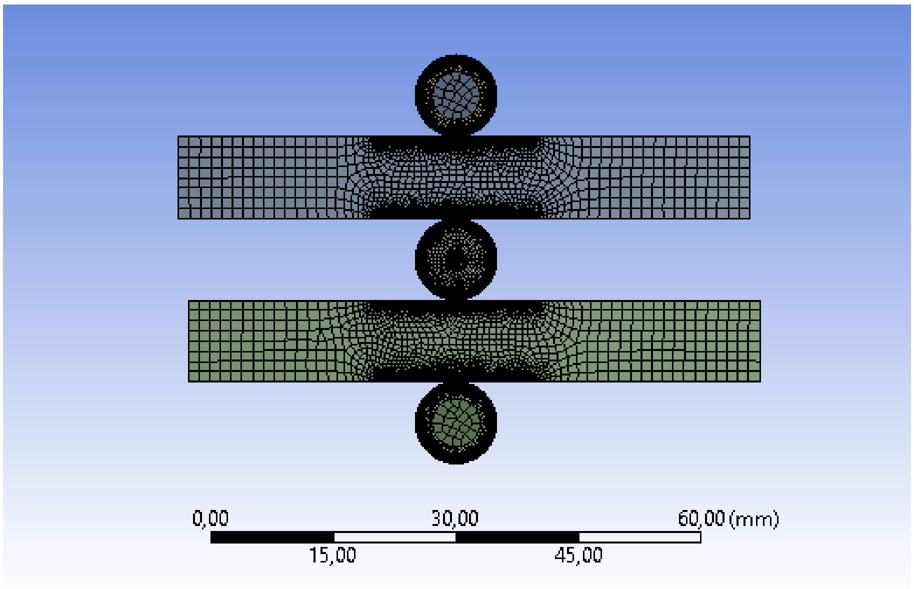

Figure 4.5: Image of all meshed components in the complete model of the NCD friction drive.

The contacts between the rods and shafts were all of the type *frictional*, which in Ansys means that if the shear stresses exceed a certain value sliding occurs, just as the equation for static sliding implies, see eq. (2.15) [17]. The frictional coefficient was varied between 0.1 and 0.3 for different simulations. The contact type between the shafts and their inner help geometry in the form of cylinders was *Bonded* to simulate that the two bodies in each set in fact were one. The setting *Trim contacts* was set to *off*. The trim contact feature reduces the number of elements in contact to speed up the solver [17]. Since the number of contact elements are crucial to obtain a valid solution, it is important that no trimming of contact elements is done.

The *Interface treatment* between each shaft and rod was set to *Adjust to touch*. In the Design Modeler module in Ansys, the interface between the geometric shapes can be interpreted to have a small geometric gap or penetration, even though they are constrained to be tangent to each surface. This can lead to poorly constructed contact areas, which can be prevented if the setting *Adjust to touch* is used. All frictional contact areas were also set to *off* when it comes to *small sliding* in the case where the rods are fixed. The reason for this is rather self explanatory, the rotation of the driving shaft when the rods are fixed leads to large amount of sliding. The default setting for small sliding is *Program controlled*, which in many situations mean *on*. This can lead to convergence problems if the amount of sliding is in fact large. Even for the case where the whole system is able to move, the *small sliding* setting was set to *off*. There should not be a large amount or sliding in this case, but the relative rotation of the parts lead to convergence issues if the sliding is assumed to be small in this case as well. For this reason, *small sliding* was always set as *off*.

The model was meshed with focus on the edges where rolling contact occurred. A mesh convergence analysis was made to ensure that the result was independent of mesh size. This was done by refining the element size until the result did not differ more than a few percents.

For the shafts to be able to rotate, a *remote displacement* was placed in the centre of each help cylinder inside each shaft. These remote displacements worked as joints. They were all locked in the x-direction but free to move in the y-direction and to rotate around the the z-axis. The coordinate system and the boundary conditions are shown in figure 4.6. Regular displacements were placed on the short sides of the rods. The displacements were locked in the y-direction to prevent that the rods were tilted during loading. In the case where reaction forces were to be examined, the rods were fixed in the x-direction at one short edge on each rod. This was also the edge where the reaction force was evaluated after solving the model. In the case where the rolling behaviour was to be analysed, the displacement in the x-direction was set to *free.*

The NCD friction drive is, as earlier mentioned, brought together with a compression force working in opposite directions on the bearing shafts. In the Ansys Workbench model the forces were applied in the y-direction on the inner help cylinders of each bearing shaft. The magnitude was ramped to the maximum value during the first step of the simulation. The magnitude varied between approximately 650 N and 1900 N in different simulations, but always with the same magnitude in opposite directions. In the second step, when the force is kept constant at maximum magnitude, the remote rotation displacement placed in the driving shaft is rotated around the z-axis a couple of degrees. This way the reaction force in the rods could be extracted for different combinations of friction coefficients and applied force.

Some other analysis settings that were adopted in the model was that the substep setting was changed from *Auto Time Stepping* to manually change initial substeps to 50, minimum substeps to 10 and maximum substeps to 100 for both simulation steps. This made it easier for the solver to converge. The setting *Large Deflections* was turned *On* to assure that the change of orientation of the elements were taken into account when solving the model [17]. In the *Nonlinear controls* menu *Newton-Raphson*

Option was set to *Unsymmetric* due to a warning message from Ansys. According to the message the friction was larger than 0.2, which lead to slow convergence. This can be a result of the high friction coefficient on the surfaces leading to an asymmetric stiffness matrix. The change of Newton-Raphson option sped up the solution significantly.

Both *augmented Lagrange*, *pure penalty* and *normal Lagrange* were used to formulate the contact in different simulations, together with both asymmetric and symmetric behaviour. It was found that the difference was minimal between these settings, so in the final version augmented Lagrange and symmetric behaviour was chosen.

The model was, as previously mentioned, partly used for observing the motion of each component and identifying any multi axial stresses when rotating. It was also partly used for creating a curve which showed which compression force was required for which frictional coefficient of the surfaces to obtain a horizontal force of 150 N, see figure 4.7. The applied force and coefficient of friction was altered in different combinations that yielded 150 N horizontal force with an error less than 1%. The reaction force could differ between 149 N and 150 N and still be accepted.

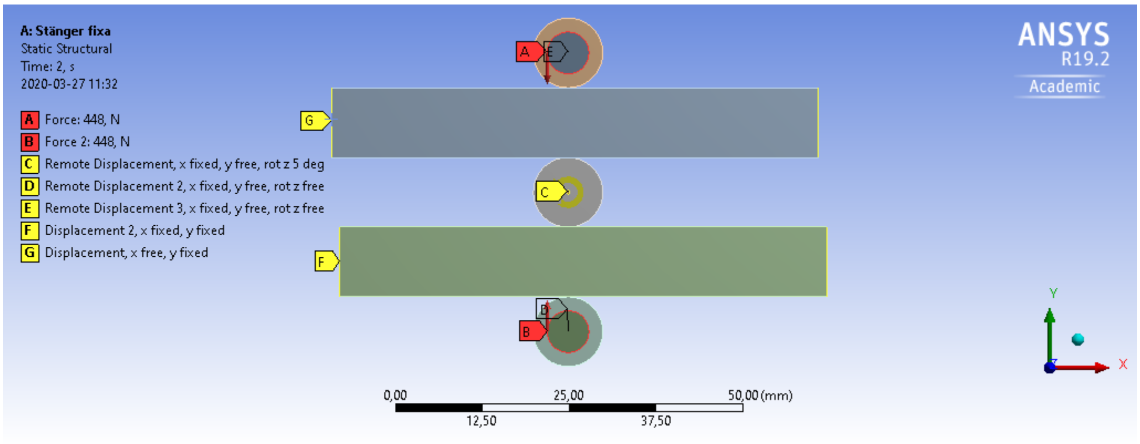

A: Stänger fixa
Static Structural
Time: 2, s
2020-03-27 11:32

A Force: 448, N
B Force 2: 448, N
C Remote Displacement, x fixed, y free, rot z 5 deg
D Remote Displacement 2, x fixed, y free, rot z free
E Remote Displacement 3, x fixed, y free, rot z free
F Displacement 2, x fixed, y fixed
G Displacement, x free, y fixed

Figure 4.6: Illustration of the fixed model setup for Ansys Workbench simulations including boundary conditions and forces applied.

With this setup, the model was verified by suppressing the two bearing shafts and one of the rods, leaving just one rod and one rotating shaft. This setup is more similar to the theoretical model given by eq. (2.15). The result of this verification showed that the model followed the theoretical model within a very small error, less than 3%. It could therefore be assumed that the complete model behaved reasonable as well. Other verification methods were also performed. Apart from a mesh convergence analysis, the normal stress in the y-direction at the end of the first step was compared to the theoretical Hertzian stress, see section 2.1. This too showed small errors, less than 2%.

The final graph with the results of which compression force is necessary for which friction coefficient to obtain a 150 N friction force is presented in figure 4.7 together with the theoretical graph of one roller with one contact surface, obtained by using eq. (2.15). It is evident that there is a rather large difference between values in the two graphs. However, the shape of the graph for the model, although rough, is almost identical to the theoretical shape, which also can be seen as a form of verification of the model. The most similar shape is found at friction coefficients between approximately 0.15 and 3. The last and most important verification of the model was made through two practical tests, described in section 5.

Observing the plotted result in figure 4.7, it can be seen that the blue graph is approximately 20% higher than the red. That is why it is suggested that the compression force required for the 150 N horizontal force is calculated with the modified Coulomb's friction as

$$F_x = 1.2\mu_s P \tag{4.2}$$

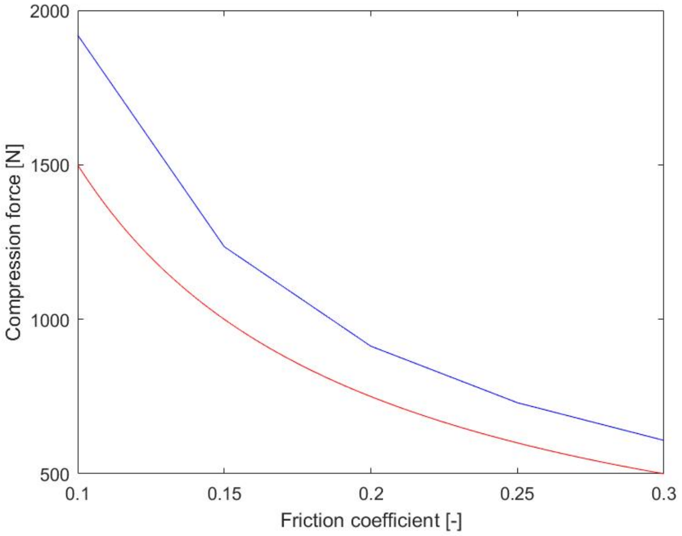

Figure 4.7: Plot of the required compression force given which surface friction coefficient to obtain a 150 N horizontal reaction force. The blue plot is based on the simulations and the red plot is the theoretical result for one contact surfaces using eq. (2.15).

As previously mentioned, the same model but with free rods in the x-direction was used for identifying how the stresses behaved in a fully dynamic system. The reason for this was to determine if the fatigue calculations should include stresses in multiple directions or if the fatigue load could be approximated as uniaxial. The setup for the free model is presented in figure 4.8.

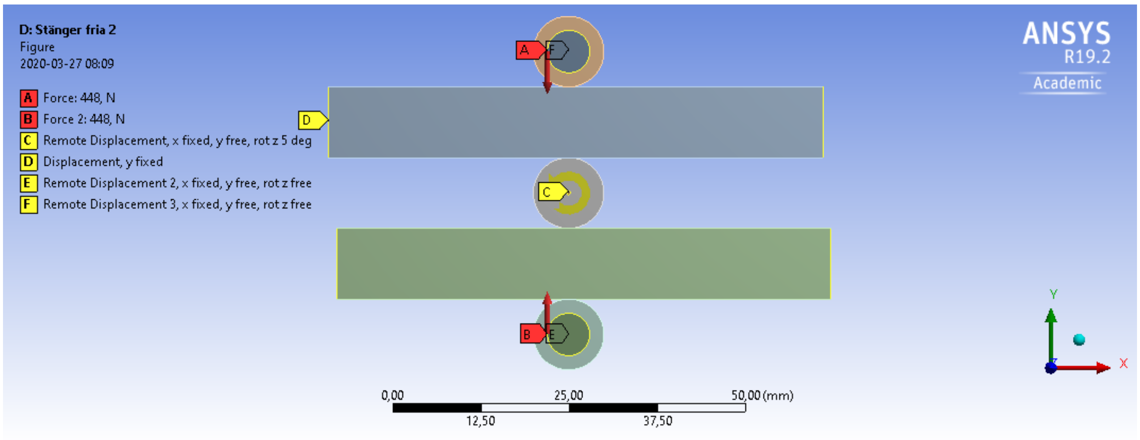

D: Stänger fria 2
Figure
2020-03-27 08:09

A Force: 448, N
B Force 2: 448, N
C Remote Displacement, x fixed, y free, rot z 5 deg
D Displacement, y fixed
E Remote Displacement 2, x fixed, y free, rot z free
F Remote Displacement 3, x fixed, y free, rot z free

Figure 4.8: Illustration of the setup for the free moving model used in the Ansys Workbench simulations including boundary conditions and forces applied.

The model was solved for several points on the simulation result curve in figure 4.7. The result showed that the normal stresses and shear stress was not necessarily affected by the rotation. The stresses remained approximately the same through out stage 1 and stage 2.

4.3 Modified Roller Profiles

ASSA ABLOY has expressed concerns about the NCD friction drive being exposed to uneven stress concentrations in the the preliminary design. Especially the contact surface between the rods and the bearing shafts could be exposed to high loads at the edges. A reason for this can be that the device that is used to apply the compression forces on the friction drive unit is placed on both sides of the bearing shafts, creating a slightly arched profile, which can create high stresses at both edges, see figure 4.9a. If a crowned roller were to be used instead, it could mean that the contact surface would be centred and more spread out, avoiding high stress concentrations on the edges, see figure 4.9b. An illustration of a crowned roller is shown in figure 4.10.

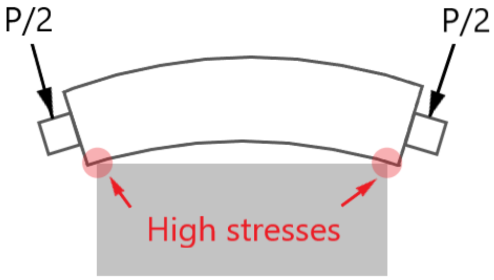

(a) Bearing shaft with straight surface.

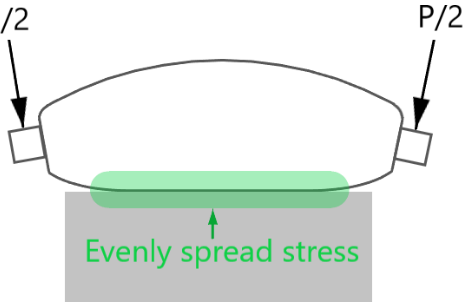

(b) Bearing shaft with crowned surface.

Figure 4.9: Illustrations of how excessive deformation of the bearing shafts can look like when exposed to forces near the edges for two different geometries.

Another reason for high stresses at the edges can be that if the rod is slightly wider than the length of the bearing shaft or vice versa, the sharp edges can lead to high stresses when load is applied, due to the area on which the force works is close to zero in these regions. Even if the edges are slightly rounded in the model, the stresses at the edges can be very high. A simple static 3D model was made in Ansys Workbench to visualise this problem, shown in 4.10. Two symmetry planes were used to reduce computational time and power. It is important to remember that this model represents one of the rods and a bearing shaft, not a driving shaft. Since the force acting on the driving shaft is more evenly distributed than the forces on the bearing shaft, the edge stresses on the driving shaft are most likely lower than the simulation results shows.

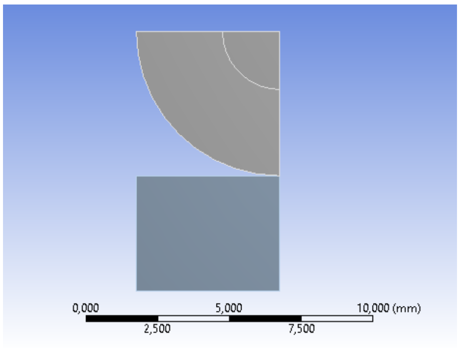

(a) Model from front.

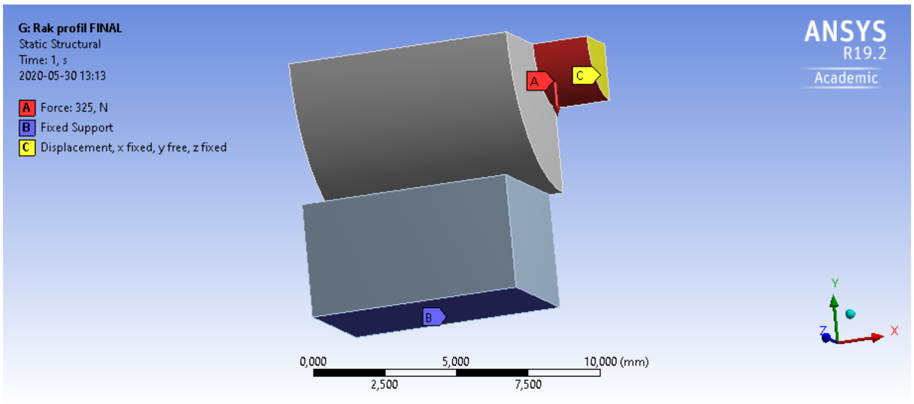

(b) Model with boundary conditions and forces.

Figure 4.10: Image of the model used for simulating edge stresses and the effect of different profiles.

The occurance of the high stresses at edges due to bending was explored with Ansys Workbench. It is known that higher stresses at the edges of a roller or a plane body can lead to a significant decrease in fatigue life, but it is usually not included in any calculation model for fatigue life [18]. Even the regular Hertzian contact formula have shortcomings when it comes to this phenomena. Hertzian contact pressure formulas only give expressions for an even stress distribution between a straight cylinder and a plane half space. But in reality the contact stress at the edges can be almost twice as high as the stresses in the middle of the cylinder [19] [20].

It is found that higher edge stresses could reduce the lifetime by approximately 30% [18]. In other words, the high stresses at the edges has to be corrected to obtain a satisfactory life. This correction can be done by changing the profile of the roller. The profile can for example be fully or partially crowned, which means that either the whole profile is circular with a very high radius compared to the roller diameter or the two ends of the roller has a circular profile while the middle part is straight, see figure 4.11.

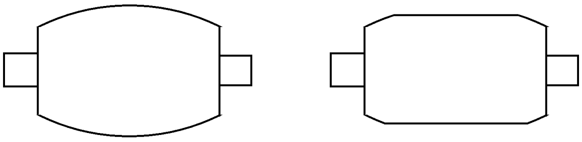

(a) Fully crowned (b) Partially crowned

Figure 4.11: Illustrations of a fully crowned roller and a partially crowned rollers.

The profile can also be for example logarithmic, elliptical or chamfered. In this Master's thesis, only fully circular crowned and logarithmic profiles will be considered, as well as a straight profile. The biggest problem when using a circular crowned or a logarithmic profile for a roller is that the contact stresses in the middle becomes higher. It is therefore not as easy as choosing a crowned roller instead of a straight, but the profile types and parameters has to be closely considered to obtain low edge stresses but not too high stresses in the middle. There are several ways to design a logarithmic profile on a roller, but in this Master's thesis the rather simple expression, $y(x) = Cln(x)$, will be used and the coefficient, C, will be changed in different version to obtain a result that minimises edge stresses. The same goes for the radius of the circular profile, see definitions in figure 4.12.

Different stress distributions for different roller profiles are discussed in [18]. It is shown that for very high loads it is difficult to eliminate the stress concentrations at the edges altogether, but at low to medium loads the logarithmic profile yields the best result if the objective is to decrease edge stresses and still have rather evenly distributed stresses along the roller with the longest contact length possible. A fully crowned roller with a large radius of curvature (150 times the cylinder diameter) also yield a rather good result in [18].

In [19], it is also shown how more realistic stress distribution along the length of the cylinder can be obtained with FEA. According to these results the edge stresses can be up to twice as high as the stresses in the middle of the contact surface and between 50% and 70% higher than the theoretical Hertz stress. Again, these models are not directly applicable on the NCD friction drive due to the difference in geometry and placement of forces, but it is a valid proof that edge stresses are a problem. The simplest profile, except for the straight cylinder, explored in [19] is the fully crowned, circular profile. It has some advantages and disadvantages. Just as all other modified profile the advantages include that it is effective when eliminating high stresses at edges but the disadvantages are that it creates a higher stress in the centre of the contact instead. The FEA also show that the circular profile is sensitive to misalignment, which can mean that the design modifications made when using a circular profile instead, in fact can lead to higher edge stresses on one side [19]. However, it is possible to find a circular profile which allows some edge stresses in order to get a lower contact pressure in the middle of the roller. In reference [18] and [19] the logarithmic profile yields a significantly lower stress in the middle of the roller and a more evenly distributed stress along the roller than a circular profile. However, just as the circular profile, the logarithmic profile is very sensitive to misalignment, risking the modified profile to do more harm than good.

4.3.1 Ansys models of roller profiles in 3D

Even though the references [19] and [18] provided valuble insights, they were not directly applicable on the NCD friction drive. That is why a complete model of one rod and one bearing shaft, in 3D was made in Ansys Workbench, which could identify high stresses and the best profile geometry. No rotation of the driving shaft was imposed, since the rotation didn't have any significant effect on the stresses. Only the static problem was considered, to identify differences between the theoretical Hertzian stresses and higher stresses at the edges. The models were made with the vertical force of 1300 N in total. The placement of the force is presented in figure 4.10.

The stresses at the edges are very high and will later be used in fatigue life calculations to show the negative effects if the profile is not changed. The normal stresses for the x-, y- and z-directions are plotted as functions of distance from the outer edge for the simplified NCD friction drive along the line of contact in Appendix A, figure 8.2-8.4 together with the equivalent stresses along the line of contact. The two best profiles are presented in table 4.1 together with the results from the straight profiles. The description of the different dimensions of the profile can be seen in figure 4.12.

It becomes evident that the straight profile has too high stresses at the edges of the rod. It also becomes clear that the logarithmic profile yields a lower compressional stress for the bearing shafts than the circular profile, but a higher stress for the rods. There is no unanimous conclusion which one of the two modified roller profiles is the best. Both reduces the edge stresses of the rods significantly. Since the bearing shafts are exposed to more loading cycles at each point than the rods, it can be argued that it is more important to reduce the stresses at the bearing shafts. That is why the logarithmic profile will be chosen as the preferred alternative.

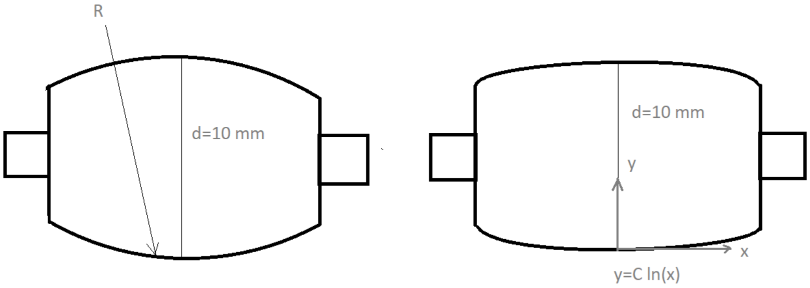

Figure 4.12: Illustration of the dimensions of the circular (right) and logarithmic profile (left) used when modelling the rollers.

Table 4.1: Result of optimizing the roller profiles.

Profile	**Component**	**Max compressional stress [MPa]**	**Stress in the middle of the component [MPa]**
Straight	Shaft	-1352	-500
	Rod	-2182	-460
Cricular, R=14 m	Shaft	-1240	-588
	Rod	-1205	-381
Logarithmic, C=0.0014	Shaft	-1167	-746
	Rod	-1315	-710

The stress distribution along the contact length for all three roller profiles are shown in Appendix A, figure 8.2-8.4. There, it can be seen that the maximum normal stress occurs at the edge for all profiles. This is due to the difficulty of eliminating edge stresses altogether for high loads. One simulation was made with a straight roller profile but with a longer contact length of 25 mm, to see how the stress distributions were affected. With Hertzian contact theory, discussed in section 2.1, the stress should decrease. However, due to the placement of the forces, the deflection of the longer bearing shaft is greater and leads to that only the outer parts of the shaft are in contact with the rod. This, of course, leads to even higher stresses at the edges. This means that increasing the contact length can lead to bigger problems if the design is not modified to decrease the deflection.

As previously mentioned, it is not uncommon that the edge stresses are twice as high as the highest normal stress in the middle of the contact surface and between 50% and 70% higher than the theoretical value [20] [19] [18]. These expressions, eq. (4.3) and (4.4), were used for verifying the accuracy of the straight roller model.

$$\sigma_{edge} \approx 2\sigma_{middle} \tag{4.3}$$

$$\sigma_{edge} \approx 1.5 - 1.7\,\sigma_{theory} \tag{4.4}$$

The different stresses of the rod in the straight profile was compared. The edge stress is -2182 MPa and the stress of the middle of the rod is is -460 MPa. The edge stress is almost 4.7 times higher than at the middle of the rod, which makes it clear that it does not follow the usual ratio from eq. (4.3). The bearing shaft edge stress is approximately 2.7 times higher than the edge stress, which is closer to fitting eq. (4.3). However, these relations are results of solving models where the compression force was placed on the entire surface of the cylinder, not at the edges. That is why the straight roller model was solved again with the force placement changed to the top surface of the bearing shaft instead. This gave a result that fitted eq. 4.3 and 4.4 better. This simulation showed that the rods experienced approximately -731 MPa normal stress in y-direction at the middle of the rod, while the edge stress was approximately -1417 MPa. This also is more similar to the stresses that the driving shaft experiences, because of the placement of the forces. The edge stress is approximately twice as high as the one found at the middle. With a contact length of 15 mm and the diameter of the straight cylinder shaft set to 10 mm, the theoretical Hertzian contact stress was calculated to 779 MPa according to eq. (2.10) and (2.9) when the compression force is 1300 N. This means that the edge stress is approximately 1.8 times higher than the theoretical Hertzian stress, which is outside the scope of eq. (4.4). This indicates that the straight profile model may not be completely accurate, but it can still be considered to be reasonable. The bearing shaft follows the relations eq. (4.3) and (4.4) rather well, with the edge stresses being approximately twice as high as the stresses in the middle and 1.4 times higher than the theoretical Hertzian stress. In general, the accuracy of the straight roller model is hard to verify completely, but according to the comparisons above, it can be determined that the model is reasonable. Since the circular- and the logarithmic roller profile models are based on the same settings as the straight roller model, it can be assumed that these are reasonable as well.

4.3.2 Crowned roller's effect on creep ratio

As described in section 4.1, the creep ratio is of less importance in this Master's thesis. However, the creep ratio for the modified rollers are calculated to ensure that it does not result in a major increase and is still of minor importance.

Since the distribution of stress and the maximum contact pressure changes when the roller profile is modified, this of course changes the creep ratio (see section 2.2). The maximum contact pressure p_{max} is no longer constant along a straight line, but varies. The contact length however, is 15 mm for all three profiles.

As mentioned in the section 2.1, the theoretical maximum Hertzian contact pressure and stress for an elliptical contact can be difficult to calculate correctly if the value of θ^* is low. This means that if the main diameter of a crowned cylinder is much smaller than the profile radius, then the half axes of the contact surface cannot be properly determined using eq. (2.3)-(2.6). For example, with the basic material data in table 4.2, the main diameter of 10 mm and a profile radius of 1 m, the value of θ^* is approximately 8°, which is already outside of the table, see Appendix A, table 8.1. For that reason, a theoretical contact half width is calculated, where all roller profiles are approximated as cylinders eq. (2.7). This half width will then be used in the expression for creep ratio for a contact with arbitrary shape eq. (2.43). Both the logarithmic and the circular profile have the approximate contact half width of 0.0709 mm with this assumption, see eq. (2.9), which yields the creep ratio -0.000673 when P=1300N and μ_s=0.2. The straight cylindrical roller with the same loading and friction coefficient is calculated to be -0.000887. There is a difference in creep ratio, but in this case both creep ratios are so small that they can be neglected and it can be assumed that the contact region is in pure stick.

4.4 Fatigue Calculations

The NCD friction drive contains of five main components. The two rods will be driven back and forth, which means that during one opening or closing, each point of a rods is exposed to one load cycle. The driving shaft, on the other hand, will be exposed to additional load cycles per opening or closing. Imagine that the curved doors has a length of 1 meter each and are connected to the rods with double the length, see figure 1.2. If the driving shaft has a diameter of 10 mm (and therefore a circumference of 10π mm) and is exposed to a load on both sides, from both rods, the driving shaft will be exposed to over 130 load cycles per opening or closing ($2 \times 2000\,mm/10\pi\ mm \approx 130$). The bearing shafts will be exposed to half the number of cycles because of the single contact surface. The rods however, can be exposed to other types of loads such as bending due to their weight or due to oscillations when moving. These types of loads will not be included in the fatigue calculations.

In theory, the normal stress in y-direction should be the same as in z-direction when z=0, see eq. (2.13)-(2.14). Even though the applied load generates multiaxial stresses, the fatigue calculations will be made assuming uniaxial stresses. There is some difficulties calculating fatigue life with multiaxial stresses when $\sigma_m \neq 0$. There can be large differences between different models and the knowledge about which model is suitable for which problem is small [21]. This is why the fatigue calculations are simplified and only the highest compressional stress from the simulation results are used. Taking the multiaxial stresses into account would most likely lead to a longer fatigue life in theory, but not necessarily in practice. Also, as discussed in section 4.2.1, there is no significant difference between the stresses when only the load is applied and when both the load and the rotation is applied. This is the why only the results from a static model, see table 4.1, are used in the fatigue calculations.

To show how different modifications of the NCD friction drive affect the fatigue life, five different scenarios will be considered. Only the fatigue of the bearing shafts and the bearing shaft side of the rods will be considered, since the stresses are the highest in these components and most likely to fail because of fatigue. If the fatigue calculations point to that the bearing shaft and its associated rod surface has a high fatigue life, it follows that the driving shaft and its associated surface has an even higher fatigue life. The fatigue behaviour of the driving shaft and the driving shaft side of the rods will be evaluated from practical tests instead of theoretical calculations, see section 5.

In the first scenario no specific modifications have been made. The rollers are straight, the material is an ordinary structural steel and no surface treatment has been made. This is the scenario that is most similar to the tests that has been made already in the NCD friction drive test rig. In scenario 1, both the edge stresses and surface roughness are higher than in theory. In scenario 2 the geometry will be the same, but the material and surface treatment are changed to material combination A, so that the component has a better resistance to fatigue. The material combination A is the steel SS 2940-03 and the surface treatment is gas nitriding, see table 4.3. More about this material and surface treatment is presented in section 3.3. In scenario 3 the material is changed to material combination B, which is also presented in greater detail in section 3.3. The material data for material combination B, steel SS 2541 with Corr-i-dur, is presented in table 4.4. In scenario 4, the material is the same as in scenario 1, but the geometry is modified to reduce the stresses and thereby improve the fatigue life. In this scenario the roller profile is logarithmic, but the result can, as a rather good approximation, apply to the circular profile as well. In scenario 5, both the best material and the best material combination is used. A summary of the results can be seen in Appendix A, table 8.2.

4.4.1 Fatigue life scenario 1

It is not known exactly which material was used for the previous tests. In this scenario it is therefore assumed that the material is the steel SAE 1045. The material data is presented in table 4.2. The coefficient of friction was never evaluated experimentally and is assumed to be μ_s=0.3, with a roughness Ra 40% higher than if the surfaces were smooth laboratory specimens. This is only based on the appearance of the surface of the rods after cyclic loading. The 40% higher roughness is only an estimation.

Table 4.2: Material data for scenario 1

E	200 GPa
σ_Y	634 MPa
b	-0.095
σ'_f	1227 MPa
σ_e	414 MPa

In the first step of calculating the fatigue life for the first scenario, the shakedown is evaluated with eq (2.47) and the shakedown diagram, see Appendix A, figure 8.1. The theoretical maximum compressional stress using the equations in section 2.1 yield the result of approximately -779 MPa. However, the more realistic value is obtained when edge stresses are considered. Using the result from the Ansys simulations, the maximum compressional stress in the rods is -2182 MPa and the minimum compressional stress is assumed to be zero. The maximum compressional stress on the driving shaft is -1352 MPa. An illustration of the approximate cyclic loading is shown in figure 4.13. The shakedown is calculated as p_{max}/k with $k = \sigma_Y/\sqrt{3}$ and result in approximately 6.0 for the rods and 3.7 for the shaft. Reading the diagram in Appendix A, figure 8.1 for μ_s=0.3 it becomes clear that the NCD friction drive experiences stresses above the shakedown limit for both the rods and the shaft and is therefore at risk of accumulative damage.

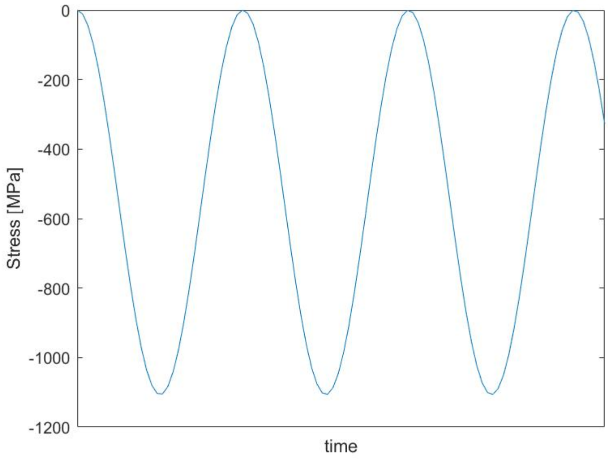

Figure 4.13: Schematic plot over how the stress in the rollers vary with time due to rotating of the rollers.

In the next step, the general fatigue life is calculated. The mean stress and stress amplitude for the rod is $\sigma_a = (0 - (-2182))/2 = 1091$ and $\sigma_m = (0 + (-1117)/)2 = -1091$. With Morrow's relation eq. (2.46) the fatigue life is calculated as

$$N_f = \frac{1}{2}\left(\frac{1091}{1227 + 1091}\right)^{-\frac{1}{0.095}} = 1394\,cycles. \tag{4.5}$$

To show the effect of the rather high surface roughness, the number of cycles to failure is modified with eq. (2.49). The modified Ra is 40% higher than the smooth specimen, which yield the relation

$$\frac{N_{f,mod}}{N_f} = \left(\frac{Ra_{mod}}{Ra}\right)^{-0.1166} \Longrightarrow N_{f,mod} = 1.4^{-0.1166} N_f = 1340\,cycles \tag{4.6}$$

This is a very low number of cycles to failure and the effect of the surface roughness is rather low. The decrease in cycles to failure due to the surface roughness is only approximately 4%. This means that the effect of surface roughness can be neglected in future tests and calculations. The fatigue life for the shafts is calculated in the same way and result in $N_f = 25908$ cycles.

Usually ASSA ABLOY want to dimension their product to survive one million cycles before failure. Since the Morrow relation, eq. (2.46), does not consider where on the body or how the material is exposed to the cyclic loading it is a good idea to calculate ratcheting as well.

Using the equation for calculating the ratcheting life eq. (2.48) is, as previously mentioned, difficult as the constant, ϵ_c, is hard to obtain without extensive practical tests. For this scenario, where the material is unknown but assumed to be a normal structural steel with rather rough surface, it can be assumed that the constant can be approximated to be the same as in rail steel BS11, which is 11.5 [8][22].

The axial strain range on the plane that experiences the highest value of strain is 0.00945 while the corresponding shear strain is 0.0147 for the rod. Both taken from the result file of the Ansys Workbench simulations. The axial strain- and shear strain range for the shaft is 0.00591 and 0.00729, respectively. The ratcheting fatigue life for the rod is calculated as

$$N_f = \frac{11.5}{\sqrt{0.00945^2 + (0.0147/\sqrt{3})^2}} = 905\,cycles \tag{4.7}$$

while the corresponding ratcheting life for the bearing shaft is

$$N_f = \frac{11.5}{\sqrt{0.00591^2 + (0.00729/\sqrt{3})^2}} = 1585\,cycles \tag{4.8}$$

It becomes evident that the rod will eventually fail of ratcheting fatigue failure and the shaft will fail of LCF. If one opening or closing corresponds to approximately 65 loading cycles for the bearing shafts and the night closing door is opened and closed once a day, the NCD friction drive will only survive approximately one and a half weeks before failure.

However, it can be that the edge stresses have little influence on the number of cycles to failure. It can be that the stresses in the middle of the components are much more important. This is evaluated by using the same expressions previously used in this scenario, but using the stresses in the middle of the shaft instead, see table 4.1. The stress in the middle of the rods and the shaft is similar enough that only the shaft has to be evaluated. With $\sigma_a = 250$ MPa and $\sigma_m = -250$ MPa, Morrow's retaltion, eq. (2.46), gives

$$N_f = \frac{1}{2}\Big(\frac{250}{1227+250}\Big)^{-\frac{1}{0.095}} = 6.6 \times 10^7\,cycles \tag{4.9}$$

the shakedown for the middle of the shaft is calculated in the same way as before, which result in $500/(634/\sqrt{3}) = 1.4$. This is way below the shakedown limit when $\mu = 0.3$, see Appendix A figure 8.1. In other words, in this scenario some regions will experience ratcheting and fatigue for a very low number of cycles, while some regions can be considered to have infinite life.

4.4.2 Fatigue life scenario 2

In the second scenario, the objective is to evaluate how the fatigue life of the straight roller is affected of the change of material and surface treatment with combination A. The material combination is steel SS 2940-03 and the hardness of the surface is 1100 HV after the surface treatment for both the rod and the shaft. The new material data is presented in table 4.3. The fatigue parameters for the material was not easy to find. That is why some of the parameters are estimations. For example, the Young's modulus, E, for most metals is approximately 200 GPa and hence this is used in the calculations. The yield stress, σ_Y, and endurance limit σ_e were taken from a material database and the untreated hardness was taken from [15]. However, the fatigue strength component, b, and the fatigue strength coefficient σ'_f had to be assumed to be equal to the corresponding data of material SAE 1045 in scenario 1, see table 4.2. With eq. (2.52), some of the material parameters in the table are modified due to the increased surface hardness.

Table 4.3: Material data for scenario 2, combination A.

E	200 GPa
σ_Y	600 MPa
b	-0.095
σ'_f	1227 MPa
σ_e	390 MPa
Hardness	290 Hv
Modified hardness	1100 Hv
Modified σ_Y	1138 MPa
Modified σ'_f	2327 MPa
Modified σ_e	740 MPa

The simulation of the straight roller profile that was presented in section 4.3.1 was ran again, but with the new material SS 2940-03. Since the stresses and strains did not change significantly in the simulation result, a simplification was made and the same stresses and strains were used in this scenario as in scenario 1.

Again, this stress was used for evaluating if the component exceeds the shakedown limit. With eq. (2.47) the shakedown is calculated as $p_{max}/k = 2182/(1138/\sqrt{3}) \approx 3.3$ for the rods and $p_{max}/k = 1352/(1138/\sqrt{3}) \approx 2.1$ for the shafts. Assuming that the friction coefficient, μ_s, in this scenario is 0.2, the shakedown can be evaluated in the diagram, Appendix A, figure 8.1. When reading the diagram, it can be seen that neither the rods nor the shaft exceeds the shakedown limit but the rods are very close to doing so.

Since no material data for the ratcheting constant, ϵ_c, is available for this material and the same strains are used, the ratcheting life calculations would yield the same result as in scenario 1. However, the LCF life of the rods was calculated. The number of cycles to fatigue based on the normal stress was calculated in the same way as in scenario 1, with mean stress and stress amplitude for the rod being the same. The fatigue life was calculated with Morrow's relation eq. (2.46).

$$N_f = \frac{1}{2}\left(\frac{1091}{2327 + 1091}\right)^{-\frac{1}{0.095}} = 83947\, cycles. \tag{4.10}$$

This is a significant improvement from scenario 1, which indicates that the choice for material has a positive impact on the fatigue life. However, the fact remains that the rods are very close to experience ratcheting at the edges.

4.4.3 Fatigue life scenario 3

In this scenario, the calculations were made in the same way as in scenario 2, but now with material combination B. Both the rods and the driving shaft assumed to be made of the steel SS 2541 and has been treated with Corr-i-dur. More about this treatment is presented in section 3.3. The hardness after the surface treatment is given by Bodycote on the order sheet. The material data is presented in table 4.4 and taken from [23] and some of the material parameters are modified with eq. (2.52).

Table 4.4: Material data for scenario 3, combination B.

E	200 GPa
σ_Y	967 MPa
b	-0.055
σ'_f	1184 MPa
σ_e	435 MPa
Hardness	300 Hv
Modified hardness	634 Hv
Modified σ_Y	1022 MPa
Modified σ'_f	1251 MPa
Modified σ_e	459 MPa

Since the Young's modulus is the same as in material combination A and the modified yield strength is approximately the same, the result from the Ansys simulation used in scenario 1 and 2 can still be used in this scenario as well.

The shakedown is calculated with eq. (2.47) as $p_{max}/k = 2182/(1022/\sqrt{3}) \approx 3.7$ for the rods and $p_{max}/k = 1352/(1022/\sqrt{3}) \approx 2.3$ for the bearing shafts. When reading in the shakedown limit diagram, see Appendix A figure 8.1, the rods exceeds the shakedown limit and the shaft does not. This means that the material- and surface treatment combination B may not be as effective as combination A. Although, it is important to remember that combination B has a better protection against corrosion, which means that it might have a longer life than combination A in some environments. The material and surface combination A should not be discarded altogether. The expression that is used to predict the yield strength, eq. (2.52), is highly uncertain and the yield strength might in reality be higher. Also, the middle of the shaft has a shakedown of $500/(1022/\sqrt{3}) = 0.85$ and the rods have a shakedown of $460/(1022/\sqrt{3}) = 0.78$, with data taken from table 4.1. These are both well below the shakedown limit, see Appendix A, figure 8.1. This means that if the ratcheting at the edges can be neglected, the rest of the components are not in danger of experience ratcheting.

4.4.4 Fatigue life scenario 4

In this scenario, the material is the basic structural steel with the same material properties as in scenario 1, table 4.2, and the roller profile is the one that yielded the best result in section 4.3.1, the logarithmic profile. The highest normal stress for the logarithmic profile is taken from table 4.1.

Again, the shakedown is evaluated and the friction coefficient is 0.3. The shakedown is $p_{max}/k = 1316/(634/\sqrt{3}) \approx 3.6$ for the rods and $p_{max}/k = 1167/(634/\sqrt{3}) \approx 3.2$ for the shaft. When comparing the value with the shakedown diagram, Appendix A, figure 8.1, it becomes evident that the shakedown limit is exceeded for both the rod and the shaft, which means that ratcheting will most likely occur at the edges of both the rods and the shaft.

The LCF is evaluated by Morrow's relation, eq. (2.46) with the stress amplitude and mean stress of the rods being $\sigma_a = (0 - (-1316))/2 = 658$ MPa and $\sigma_m = (0 + (-1316))/2 = -658$ MPa.

$$N_f = \frac{1}{2}\left(\frac{658}{1227 + 658}\right)^{-\frac{1}{0.095}} = 32389\, cycles. \tag{4.11}$$

For the shafts, which have the stress amplitude and mean stress $\sigma_a = (0-(-1167))/2 = 584$ MPa and $\sigma_m = (0 + (-1167))/2 = -584$, the fatigue life is

$$N_f = \frac{1}{2}\left(\frac{584}{1227 + 584}\right)^{-\frac{1}{0.095}} = 74595\, cycles. \tag{4.12}$$

4.4.5 Fatigue life scenario 5

Scenario 5 is based on the logarithmic roller profile and the material- and surface combination A. It is predicted that in this scenario, the components have infinite life. It is therefore interesting to know which the highest possible compressional stress is that still yield an infinite life. This is evaluated with the help of Sodebergs equation, see table 2.1. $N_f|_{m=0}$ is equal to the endurance limit σ_e. The expression can be rewritten as

$$\frac{\sigma_a}{\sigma_e} + \frac{\sigma'_m}{\sigma_Y} = 1 \tag{4.13}$$

where σ_a is the maximum stress amplitude that still guarantee infinite life and σ'_m is the modified mean stress where the original cyclic stress is fully reversed with $\sigma_m = 0$ and the load ratio $R^* = 0$. The modified mean stress can therefore be described as $\sigma'_m = \sigma_a - \sigma_m$ [6]. The expression can be rewritten as

$$\frac{\sigma_a}{\sigma_e} + \frac{\sigma_a - \sigma_m}{\sigma_Y} = 1 \tag{4.14}$$

With the same stress amplitude and mean stress as in scenario 4 and the material data from table 4.3, the maximum allowed stress amplitude for the rod is

$$\sigma_a = \sigma_e \frac{\sigma_Y - \sigma_m}{\sigma_Y + \sigma_e} = 740 \times \frac{1138 + 658}{1138 + 740} = 708\,MPa \tag{4.15}$$

In other words, the highest stress amplitude allowed for infinite life is 708 MPa for the rods, while the actual stress amplitude in this scenario is is 658 MPa. There is a rather good margin for the fatigue life. Calculating the shakedown for the rod and shaft in the same way as previous scenarios, the rod has a shakedown of 2.0 and the shaft has a shakedown of 1.8. For $\mu_s = 0.2$, both the rod and the shaft are below the shakedown limit.

5 Results From Practical Tests

Practical tests were performed to verify the curve in figure 4.7, in which a relation between compression force and coefficient of friction was described for a 150 N horizontal force, see eq. (4.2). Some practical tests were also performed during a longer period of time, to evaluate the fatigue life of the driving shaft and the driving shaft side of the rods.

The first part of the test aimed at evaluating the surface friction coefficient. This was done with the principle of the tilting plane with a loose object described in section 2.2. This test provided a friction coefficient of 0.19, which appears reasonable for a steel-steel contact.

In the second part of the practical test, the motor was removed from the test rig and a lever was attached to the driving shaft. The compression force was set to -1805 N and the lever was then exposed to an increasing force until the point where the driving shaft started to rotate. The force applied right before the shaft started to rotate represents the force F_x in the expression $F_x = \mu_s P$, see section 2.2. In theory, the recorded force should be $F_x = 0.19 \times 1805 = 343\,N$. In the practical test the result was 350 N. Using the Ansys workbench model, with fixed rods, as described in section 4.2.1 and eq. (4.2), the compressional force to obtain a vertical force of 350 N is -2211 N.

It is evident that the model used for the numerical simulations failed to capture the behaviour of the cylindrical roller with two contact surfaces. In fact, the simple theoretical expression in eq. (2.15) was much better at predicting the compressional force needed, even though it only considers situations with one contact surface. Reasons for this can of course be that some mechanism in the test rig interfered with the results. For example, in the first trials, some components in the test rig pressed against the rods, creating more friction than predicted. This problem was solved and no other visually observable defect was found in the test rig. That is why the practical tests were considered more reliable than the model used for the numerical simulations. Some settings in the model probably caused by an over-estimation of the forces required for obtaining the different coefficients of friction. Since the practical test results confirmed that Coulomb's friction law, eq. (2.15), provided good results, no more time was spent on the Ansys Workbench model.

The fatigue tests were also performed in the test rig, but connected to a larger test setup with blades connected to the rods, representing the NCD blades, see figure 5.1. The material combination used for this test was material combination B, see table 4.4, and the tests ran for approximately 217,000 cycles. One cycle represents one opening or closing of the door. These tests were made mainly to observe the fatigue behaviour of the driving shaft and its associated rod surfaces. The results showed a great improvement from previous tests, discussed in section 3.2. The results from the two fatigue tests might be hard to compare on a fair level, because it is unknown how many cycles the previous test was ran for. But, setting the number of cycles aside, the surface after the tests, with material combination B, shows little or no signs of wear, see figure 5.2. Some small scratches can be seen on the driving shaft, but they are much smaller compared to previous test result, see figure 3.3. The surface roughness measurements showed that the Ra-value decreased from 1.6 μm before the fatigue tests to 0.89 μm after the tests. This can be explained by the fact that the surface asperities are worn down when the the surface is exposed to cyclic loading. As discussed in section 4.4.1, a 40% change in Ra does not significantly affect the number of cycles to failure. It can, however change the coefficient of friction.

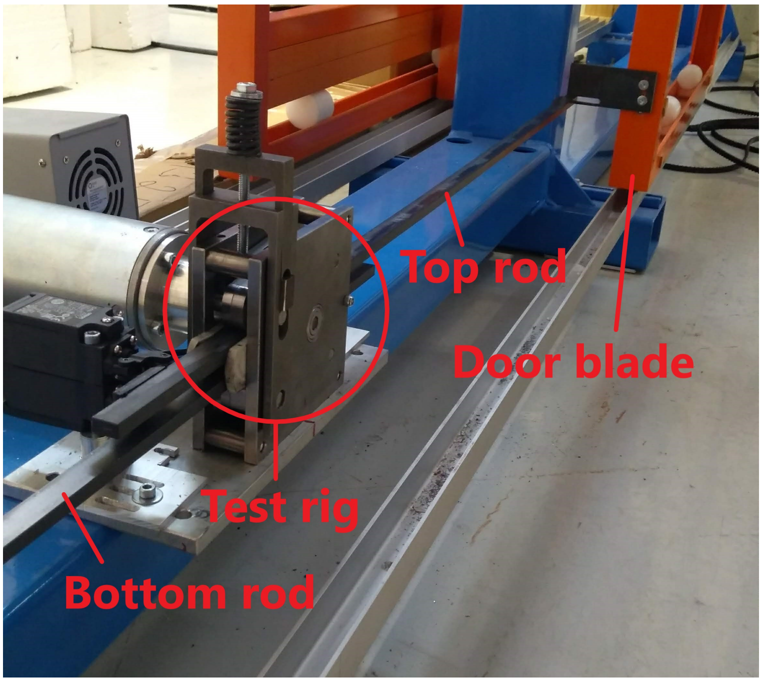

Figure 5.1: Test setup with attached door blade for fatigue tests.

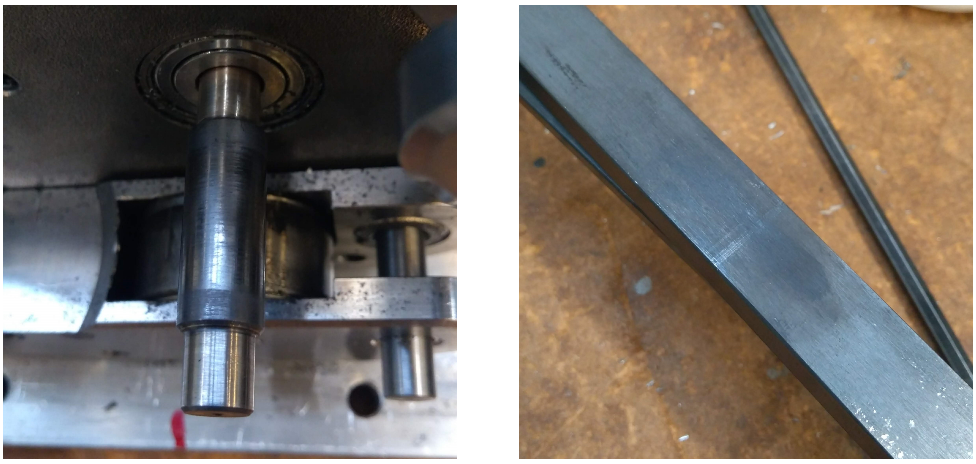

(a) Driving shaft.

(b) Rod on driving shaft side.

Figure 5.2: Surfaces of the components after the fatigue tets.

These results point to that a straight roller profile with material combination B, steel SS 2541 with Corr-i-Dur treatment, is a very good choice for the NCD friction drive, if only the driving shaft and its associated rod surfaces are considered. Material combination A might also be a good choice, but it might be unnecessary to use a material with the very hard surface of 1100 HV if the softer material combination is enough. Also, Material combination B has the advantage of higher corrosion protection. However, it is important to remember that this applies to the driving shaft and its associated rod surfaces only. Ratcheting and fatigue wear can still occur at the other sides of the rods and on the bearing shafts.

6 Future Improvements and Areas of Research

The theoretical fatigue calculations pointed to large wear at the edges of the bearing shafts and at the edges of the rods. However, no practical fatigue tests have been made in these areas to verify this. In the future development of the NCD friction drive, more fatigue tests has to be done on these components. It cannot be assumed that the practical test results from the driving shaft can be directly applied on the bearing shafts because of the difference in compression force action.

It can be a good idea to observe how the coefficient of friction is changed during cyclic loading. The surface roughness is decreased from 1.6 μm to 0.89 μm, which might change the coefficient of friction slightly, which means that the compression force has to be altered.

In this Master's thesis, the rods of the NCD friction drive have only been studied with focus on the contact surfaces. However, the rods in the final design can be several meters long. In the future, these rods should be studied and designed to not bend due to their own weight.

7 Conclusion

To summarize the findings in this Master's thesis there are certain things to consider in the future of the development of the NCD friction drive.

It is more effective to use a longer shaft and a wider rod than to increase the radius of the shafts. Both the Hertzian pressure and the creep ratio benefits from this approach, although the creep is not very important to consider in this application. It is more important to ensure that the contact surfaces of the components have entered the region where both slip and stick occurs and has left the region where there is only slip. This is done with Couloumb's friction law, $F_x = \mu_s P$. Depending on which coefficient of friction the material has in the final design the compression force has to be modified with the compression device so that the horizontal force is at least 150 N. The compression force should be between approximately between 600 N and 1000 N.

The dimensions that ASSA ABLOY wanted the NCD friction drive to have, are possible to use in the final design. Using approximately 15 mm long shafts with a diameter of 10 mm and rods with 8 mm tickness and 15 mm width provide acceptable results. The results can be improved, however, if the dimensions are increased. Although, the length of the bearing shafts has to be increased with caution since longer shafts can lead to large deflections and higher edge stresses.

A modified profile of the shafts can lead to lower stresses at the edges of all components, which can lead to a longer fatigue life. These profiles can be either circular with full crowning or they can have a logarithmic profile. Both yield a reduction of edge stresses but at high loads it might not be enough to only change the roller geometry, the choice of material also has to be revised. The best choice of material- and surface treatment combination was difficult to determine in this Master's thesis. If only the theoretical fatigue life of the bearing shafts and the bearing shaft side of the rods is considered, material combination A, steel SS 2940-03 with the surface treatment *gas nitriding* is preferable. It has a very high surface hardness, but does not have the same level of corrosion protection as, for example, a material treated with Corr-i-Dur has. If only the practical fatigue tests of the driving shaft and the driving shaft side of the rods are considered, material combination B, steel SS 2541 with Corr-i-Dur is preferable.

What is common in all calculations regarding fatigue life and ratcheting life is that they are based only on theoretical expressions. Also, the simulation results used in the calculations, although verified to the greatest extent possible, are rather uncertain. That is why much more practical testing is needed in the future development of the NCD friction drive.

References

[1] V. L. Popov. *Contact Mechanics and Friction.* Berlin Heidelberg: Springer, 2d edition, 2017.

[2] B. Broberg, G. Hedner, H. Johansson, S. E. Larsson, R. Nilsson, and A. Persson et al. Hertzkontakt. In B. Alfredsson, editor, *Handbok och Formelsammling i Hållfasthetslära.* Stockholm: Instant Book AB, 2016.

[3] R. G. Bayer. *Mechanical Wear Fundementals and Testing.* New York: Marcel Dekker, Inc., 2d edition, 2004.

[4] J. A. Williams and R. S. Dwyer-Joyce. *Contact Between Solid Surfaces.* CRC Press LLC, 2001.

[5] P. L. Menezes, S. P. Ingole, M. Nosonovsky, S. V. Kailas, and M. R. Lovell, editors. *Tribology for Scientists and Engineers.* Springer, 2013.

[6] S. Suresh. *Fatigue of materials.* Cambridge University Press, 2d edition, 1998.

[7] B. Alfredsson. *A Study on Contact Fatigue Mechanisms.* PhD thesis, Royal Institute of Technology, Department of Solid Mechanics, Stockholm, Sweden, 9 2000.

[8] J. W. Ringsberg, M. Loo-Morrey, B. L. Josefson, A. Kapoor, and J. H. Beynon. Prediction of fatigue crack initiation for rolling contact fatigue. *International Journal of Fatigue*, 22(3):205 – 215, 2000.

[9] W. Xiao, Haibo Chen, and Y. Yin. Effects of surface roughness on the fatigue life of alloy steel. *Key Engineering Materials*, 525-526:417–420, 11 2012.

[10] P. Zhang, S X Li, and Z F Zhang. General relationship between strength and hardness. *Material Science and Engineering*, 529:62–73, 2011.

[11] Bodycote. *Värmebehandlingsguide.* Bodycote, 9th edition, 2013.

[12] T. L. Carter, E. V. Zaretsky, and W. J. Anderson. *Effect of hardness and other mechanical properties on rolling contact fatigue life of four high temperature bearing steels.* National Aeronautics and space administration, Washington, 3 1960.

[13] A. Praveen Sekhar, S. Nandy, K. K. Ray, and D. Das. Hardness - yield strength relation of al-mg-si alloys. *IOP Conference Series: Materials Science and Engineering*, 338:012011, mar 2018.

[14] A. Nakonieczny and G. Monka. Contact fatigue strength of 41cralmo7 grade steel under nitriding and shot-peening treatment. *Material Science*, 48(6):715–721, 5 2013.

[15] Kihlbergs Stål. *Nitrerstål.* http://www.kihlsteel.se/Nitrerstaal-2940.pdf. Checked: 2020-05-13.

[16] Bodycote. Corr-i-dur, 2019. https://www.bodycote.com/sv/tjanster/varmebehandling/nitrerprocesser/corr-i-dur/. Checked: 2019-02-26.

[17] Ansys. *Mechanical user guide*, 19 edition, 2020. Retrieved online: 2020-03-05.

[18] F. B. Oswald, E. V. Zaretsky, and J. V. Poplawski. Effect of roller geometry on roller bearing load–life relation. *Tribology Transactions*, 57:928–938, 2014.

[19] M. Duchemin, C. Tugui, and V. Collee. Optimization of contact profiles using super-ellipse. *SAE International Journal of Materials and Manufacturing*, 10:234–244, 2017.

[20] S. Maulik J and P.H. Darji. Fatigue life improvement through reduction of edge pressure in cylindrical roller bearing using fe analysis. *International Journal For Technological Research In Engineering*, 1:2347–4718, 2014.

[21] L. Pook. *Metal Fatigue What It Is, Why It Matters.* Springer, Dordrecht, The Netherlands, 2007.

[22] J. W. Ringsberg. Life prediction of rolling contact fatigue crack initiation. *International Journal of Fatigue*, 23(7):575 – 586, 2001.

[23] S.C. Wu, S.Q. Zhang, Z.W. Xu, G.Z. Kang, and L.X. Cai. Cyclic plastic strain based damage tolerance for railway axles in china. *International Journal of Fatigue*, 93:64 – 70, 2016.

8 Appendix A

The table for coefficients m and n for calculating half axes of an elliptical contact surface is presented in table 8.1 [2].

Table 8.1: Coefficient m and n for equation 2.6 and 2.7.

θ [°]	0	10	15	20	25	30	35	40	45
m	-	6.612	4.875	3.778	3.150	2.731	2.397	2.136	1.926
n	0	0.851	1.040	1.220	1.400	1.453	1.550	1.637	1.709
θ [°]	50	55	60	65	70	75	80	85	90
m	1.754	1.611	1.486	1.378	1.284	1.202	1.128	1.061	1
n	1.772	1.828	1.875	1.912	1.994	1.967	1.985	1.996	2.00

The diagram that is used for evaluating the shakedown is presented in Appendix A, figure 8.1. The diagram is taken from the book *Fatigue of Materials* [6] and is modified to only include relevant information.

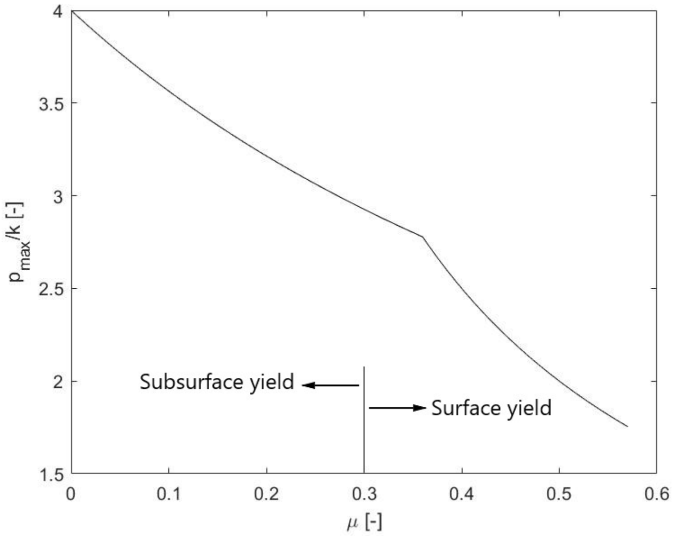

Figure 8.1: Shakedown limit for rolling of a cylinder on plane surface that includes both stick and slip region. The plot is taken from the diagram in [6].

The result from the Ansys Workbench simulations of the model for the different roller profiles were plotted along a path tracing line of contact. The stresses (normal stresses in the x-, y- and z-directions as well as the effective Von Mises stress) are plotted as a function of the distance from the outer edge. The edge of the bodies are located at a zero distance, and at distance of 8 mm for the roller and 7,5 mm for the rod, the middle of the contact surfaces are located. The stress distribution is assumed to be mirrored at the end of the plot, due to symmetry. All simulations were made with a compression force of 1300 N. The noise in the plots is mostly due to the mesh.

Even though the mesh convergence analysis was successful, some noise remained in the result. But because of the long computational time and lack of memory on the computer an even finer mesh would imply, the already converged mesh was kept.

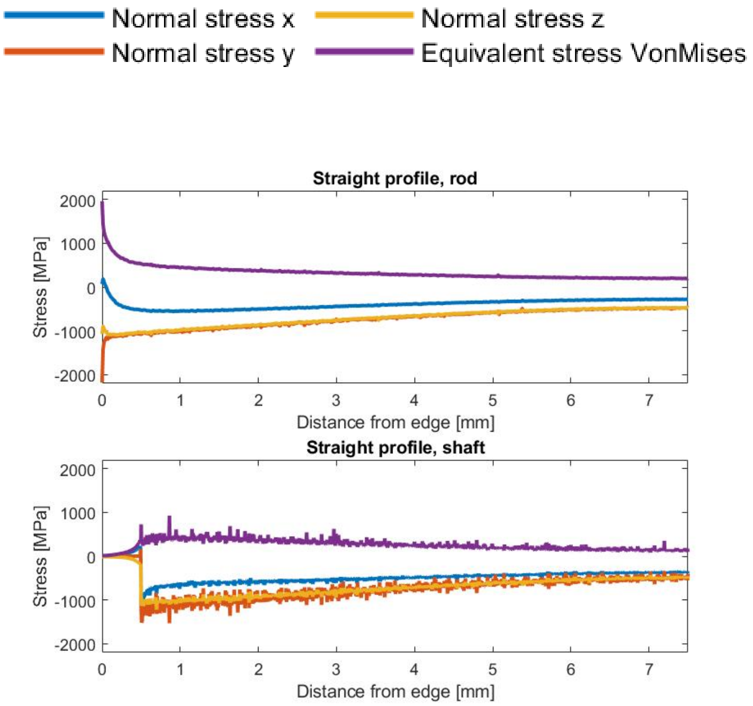

Figure 8.2: Stresses as a function of distance from the edge for straight roller.

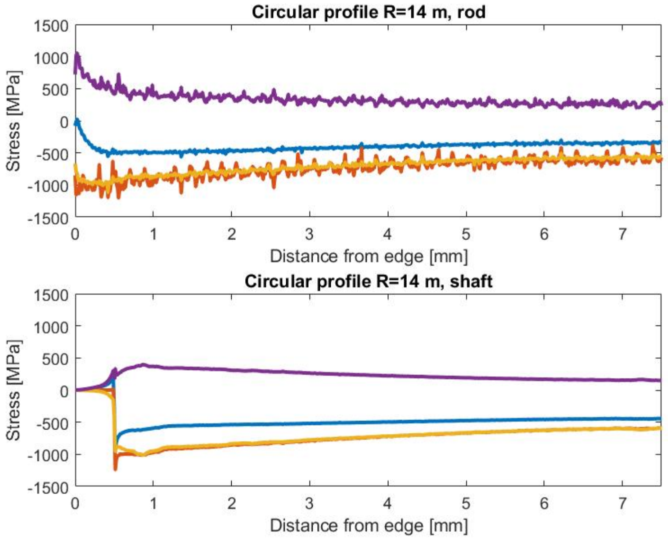

Figure 8.3: Stresses as a function of distance from the edge for roller with circular profile, R=14 m.

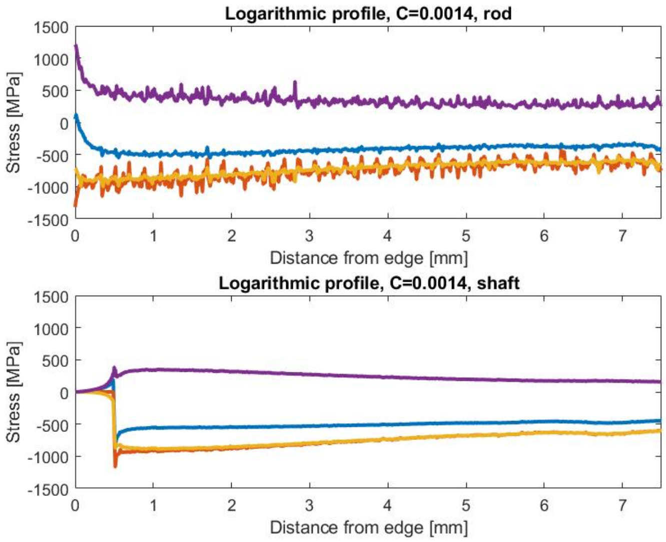

Figure 8.4: Stresses as a function of distance from the edge for roller with logarithmic profile, C=0.0014.

Table 8.2: Summary of the results from the fatigue calculations.

		Number of cycles to failure	
		Bearing shafts	Rods
Scenario 1	Fatigue	25908	1340
	Ratcheting	1585	905
Scenario 2	Fatigue	Not calculated	83947
	Ratcheting	Nonexistent	Nonexistent
Scenario 3	Fatigue	Not calculated	Not calculated
	Raticheting	Nonexistent	905
Scenario 4	Fatigue	74595	32389
	Ratcheting	Not calculated	Not calculated
Scenario 5	Fatigue	Infinite life	Infinite life
	Ratcheting	Nonexistent	Nonexistent